IDENTIFICATION OF ARTERIAL INPUT FUNCTION
IN PERFUSION IMAGING
WITH MR ANGIOGRAPHY-SUPPORTED
SEMI-AUTOMATIC METHOD

by

Bora Büyüksaraç

B.S., Electrical and Electronics Engineering, Boğaziçi University, 1997

M.S., Institute of Biomedical Engineering, Boğaziçi University, 2000

Submitted to the Institute of Biomedical Engineering

in partial fulfillment of the requirements

for the degree of

Doctor

of

Philosophy

Boğaziçi University

2018

IDENTIFICATION OF ARTERIAL INPUT FUNCTION IN PERFUSION IMAGING WITH MR ANGIOGRAPHY-SUPPORTED SEMI-AUTOMATIC METHOD

APPROVED BY:

Prof. Dr. Mehmed Özkan   . . . .
(Thesis Advisor)

Prof. Dr. Ahmet Ademoğlu   . . . .

Assoc. Prof. Dr. Burak Acar   . . . .

Prof. Dr. Yekta Ülgen   . . . .

Assist. Prof. Dr. Andaç Hamamcı   . . . .

DATE OF APPROVAL: 31 January 2018

ACKNOWLEDGMENTS

My PhD experience was significantly different than many since it took so many years. During this time, I have studied not only on my own thesis but also on different fields of biomedical engineering. It was a real pleasure for me to accomplish many projects in the Institute at Bogazici University where I always felt like home. I feel priviledged to be a graduate and a member of this community.

First, I would like to express my gratitutes to my advisor, Prof. Dr. Mehmed Özkan for his support and guidance throughout this study.

My special statements of regards go to Prof. Dr. Yorgo Istefanopulos who has initiated my career in biomedical engineering when I was an undergraduate student in Electrical and Electronics Engineering at Bogazici University. It was great for me to be a reasearch assistant when he was the director of the Institute. He has a very special place in my life and I am very lucky to be one of his students.

My special words of thanks should also go to my committee members Prof. Dr. Ahmet Ademoğlu and Assoc. Prof. Dr. Burak Acar for their time and scientific advices throughout the progress of the thesis.

I would like to thank all my friends Ahu Türkoğlu, Asım Samlı, Bige Vardar, Burcu Tunç Çamlıbel, Burteçin Aksel, Deniz Nevşehirli, Esin Karahan, Fatma Gülden Temiz Şimşek, Filiz Ateş, Gamze Bölükbaşı Ateş, Hakan Solmaz, Kazım Çamlıbel, Mehmet Kocatürk, Murat Tümer, Mustafa Kemal Ruhi, Nermin Topaloğlu Avşar, Özgüncem Bozkulak, Özgür Kaya, Özgür Tabakoğlu and Tuğba Köker. I specifically want to acknowledge Didar Talat. I am so much grateful for her sincere friendship and also for her generous help especially during the tough times of my thesis.

I also would like to thank Gaye Şentürk and Hilmi Şentürk for their valuable

friendship.

I would like to thank to Ayşegül Ünal, Çiğdem Günsür and Muhammed Avşar for their help at the administration.

This PhD would not have been possible without the support of my family. I would like to thank my mother Şenay Büyüksaraç, my father Yıldırım Büyüksaraç and my brother Can Büyüksaraç for always believing in me. Very special thanks go to my wife Güldem Büyüksaraç for her invaluable support and patience. Her encouragements gave me the energy I need throughout this study.

Finally, I would like to thank Zeynep Fırat at Yeditepe University Hospital for her generous help in MR imaging.

ACADEMIC ETHICS AND INTEGRITY STATEMENT

I, Bora Büyüksaraç, hereby certify that I am aware of the Academic Ethics and Integrity Policy issued by the Council of Higher Education (YÖK) and I fully acknowledge all the consequences due to its violation by plagiarism or any other way.

Name :

Signature:

_____

_____

Date:

_____

ABSTRACT

IDENTIFICATION OF ARTERIAL INPUT FUNCTION IN PERFUSION IMAGING WITH MR ANGIOGRAPHY-SUPPORTED SEMI-AUTOMATIC METHOD

This thesis aims to improve arterial input function (AIF) selection in DSC-MRI by using the information gathered through magnetic resonance angiography (MRA) and cluster analysis of the concentration time curve (CTC) parameters. MRA was utilized with a dual-purpose, identifying arterial locations during the parametric evaluation of CTCs in DSC-MRI, and avoiding shape distortions in AIF. The knowledge of arterial locations is essential to the research, as it guided the cluster analysis carried out with the CTC parameters of voxels located within and around the middle cerebral artery (MCA). Additionally, it enabled us to identify the voxels that meet the AIF criteria and those with distorted CTCs. The literature has developed the following criteria for selecting AIF: high peak height (PH), small full-width-at-half-maximum, (FWHM), early time-to-peak (TTP), and early arrival time (AT). However, it has been found that high PH and small FWHM may indicate a shape distortion due to partial volume effect (PVE). PVE is a common problem in AIF identification, which emerges when a voxel contains both artery and brain tissue. To avoid PVE, we included in our cluster analysis a recently introduced parameter, the SS:AUC ratio, which indicates the ratio of the mean steady state (SS) value (post-bolus equilibrium) to the area under the curve (AUC) of the first passage of contrast agent. We calculated the SS:AUC of VOF and used it as a reference in selecting AIF. By using this reference value, we managed to detect the CTCs that were not distorted by PVE. If the SS:AUC of AIF was far from the reference value, CBF was either under- or over-estimated by a maximum of 41.1 ± 14.3 and $36.6 \pm 19.2\%$, respectively.

Keywords: DSC magnetic resonance imaging, cerebral blood flow, arterial input function, MR angiography, cluster analysis, partial volume effect, middle cerebral artery.

ÖZET

PERFÜZYON GÖRÜNTÜLEMEDE MR ANJİYOGRAFİ DESTEKLİ YARI OTOMATİK METOTLA ARTERYAL GİRDİ FONKSİYONU TANIMLANMASI

Bu tez DSC-MR görüntülemede damara ait girdi fonksiyonunun seçimini MR anjiyografi ve konsantrasyon zaman eğrilerinin parametrelerini sınıflandırma yöntemi kullanarak geliştirmeyi hedeflemektedir. MR anjiyografiden konsantrasyon zaman eğrilerinin parametrik değerlendirilmesi sırasında damar lokasyonlarının tespiti ve arteryel girdi fonksiyonunda olabilecek şekil bozukluklarından kaçınmak için faydalanılmıştır. Damar lokasyonlarının bilinmesi bu araştırma için önem taşımaktadır çünkü MCA'in üzerindeki ve etrafındaki piksellere ait konsantrasyon zaman eğri parametrelerinin sınıflandırma analizinde rehberlik etme değerine sahiptir. Buna ilave olarak, AIF kriterlerine sahip olanların yanında konsantrasyon zaman eğrilerinde şekil bozukluğu gözlenen piksellerin damar lokasyonuna göre konumlarını tespit edebilmemizi sağlar. Önceki çalışmalar AIF seçimi için şu kriterleri geliştirmiştir: tepe noktasının yüksek olması, tepe noktasının yarısındaki eğri genişliğin küçük olması, zirve zamanının erken olması ve kontrast madde varış zamanının erken olması. Bunula birlikte, tepe noktasının çok yüksek olması ve tepe yüksekliğinin yarısında eğri genişliğinin çok küçük olması kısmi hacim etkisine bağlı şekil bozukluğunun göstergesi olduğu bulunmuştur. Tek bir vokselin içinde hem beyin dokusu hem damar bulunduğunda oluşan kısmi hacim etkisi, AIF seçiminde sıkça karşılaşılan bir problemdir. Bundan kaçınmak için çalışmamızda, konsantrasyon zaman eğrisinin son kısmındaki denge düzeyi ile kontrast maddenin ilk geçiş bölümünün altında kalan alanın oranı olarak tanımlanmış olan SS:AUC parametresini kullandık. AIF in SS:AUC değeri referans değerden uzak olduğunda CBF nin %41.1 $\pm$ 14.3 düşük veya %36.6 $\pm$ 19.2 yüksek hesaplanmasına sebep olduğu görülmüştür.

Anahtar Sözcükler: DSC manyetik rezonans görüntüleme, serebral kan akışı, arteryel girdi fonksiyonu, MR anjiyografi, kümeleme analizi, kısmi hacim etkisi, orta serebral arter.

TABLE OF CONTENTS

LIST OF FIGURES

LIST OF TABLES

LIST OF SYMBOLS

σ^2	Variance
Σ	Sum

LIST OF ABBREVIATIONS

3D	Three-dimensional
AIF	Arterial input function
ASL	Arterial spin labeling
AT	Arrival time
AUC	Area under the curve
BA	Basilar artery
BAT	Bolus arrival time
CBF	Cerebral blood flow
CBV	Cerebral blood volume
CT	Computed tomography
CTC	Concentration time curve
DSC	Dynamic susceptibility contrast
EPI	Echo planar imaging
FM	First moment
FWHM	Full width at half maximum
Gd-DTPA	Gadolinium diethylenetriamine penta-acetic acid
ICA	Internal carotid artery
MCA	Middle cerebral artery
MRA	Magnetic resonance angiography
MRI	Magnetic resonance imaging
MTT	Mean transit time
MPC	Maximum peak concentration
PET	Positron emission tomography
PH	Peak height
POVE	Percentage of variation explained
PVE	Partial volume effect
ROI	Region of interest
SS	Steady state

SS:AUC	Steady state area under curve ratio
TE	Time to echo
TOF	Time of flight
TR	Repetition time
TTP	Time to peak
VOF	Venous output function

1. INTRODUCTION

1.1 Cerebral Perfusion

Cerebral perfusion imaging is a technique used for measuring cerebral blood flow (CBF), with which the first passage of the contrast agent through the brain tissue is observed [1]. It indicates the blood flow in tissue capillaries, which is measured in units of "ml g^{-1} min^{-1}". The CBF measurement is approximately 60 ml and 20 ml $(100\ g)^{-1}$ min^{-1} in grey and white matter tissues, respectively, which leads to a very high grey matter-white matter contrast in CBF maps. Brain tissue health is contingent on blood supply, and perfusion deficit is a typical cause of tissue death [2]. Local increase in blood flow is associated with the cognitive function of a specific brain region [3]. Based on these findings, it can be argued that cerebral perfusion is an extremely crucial parameter, which is highly definitive of brain functioning. CBF measurement is essential to our understanding of the brain physiology, through which we can monitor oxygen and nutrients delivery to tissue and also waste removal.

There are various magnetic resonance imaging (MRI) methods for measuring CBF. The widely used techniques are dynamic-susceptibility contrast (DSC) MRI and arterial spin labelling (ASL) [4]. The non-invasive ASL technique is based on the use of magnetic labelled blood as an endogenous contrast. DSC-MRI, currently the most popular method, is carried out by injecting a paramagnetic contrast agent (a gadolinium-based contrast agent) [5]. During the passage of the bolus through the brain, transient MR signal changes are measured [1]. DSC-MRI is usually found efficient, although an exogenous MR contrast agent is injected as part of the procedure. Its advantages include short acquisition time (approximately 1 min), use of widely available MRI sequences (e.g. gradient-echo echo-planar imaging, EPI), and a superior contrast-to-noise ratio compared with ASL and perfusion computer tomography (CT). During the passage of contrast matter through the brain, there occurs a transient signal drop on T2- and T2*-weighted images. The concentration of the contrast agent, C(t),

can be inferred from this signal intensity change. C(t) is formulated by a convolution expression, as described by the kinetic theory in DSC-MRI [6, 7]

$$C(t) = CBF \cdot AIF(t) \otimes R(t) = CBF \cdot \int_0^t AIF(\tau)R(t - \tau)d\tau \qquad (1.1)$$

AIF(t), the arterial input function, is the contrast agent in time for an artery that is supposed to supply blood to the tissue of interest. R(t) is the tissue residue function, which can also be referred to as impulse response function; as the name implies, it is the function that describes the response of the tissue to an instantaneous input. R(t) indicates the fraction of the contrast agent residue in the tissue following an infinitesimally short (i.e. a delta Dirac) input function. R(0) = 1 states that initially all the contrast agent is present in the tissue, whereas R(∞) = 0 means that there is no contrast agent in the tissue after a long time. Given that AIF is composed of consecutive short boluses, the total contrast agent accumulated in the tissue at time t is given by the sum of the contributions from these short boluses AIF(τ) injected at time τ. In the same equation, R(t-τ) stands for the fraction of the contrast agent that remains at time t from each short bolus injected at time τ. The extent of concentration in tissue is determined by the amount of blood delivered to the tissue per unit time, which is expressed in the equation with the CBF factor. The quantification of cerebral perfusion involves two tasks of utmost importance: the AIF measurement and a deconvolution analysis for the removal of the temporal spread contribution of AIF from the tissue concentration time-course [6]. The literature has also used the DSC-MRI data in assessing two other crucial physiological parameters: cerebral blood volume, CBV, which refers to the fraction of the tissue volume filled with blood, and the mean transit time, MTT, which stands for the average time it takes the contrast agent to pass through the tissue vasculature. The relationship between the three perfusion parameters (CBF, CBV, and MTT) is explained by the central volume theorem as follows [8]:

$$MTT = \frac{CBV}{CBF} \tag{1.2}$$

CBV is usually measured in units of ml g^{-1}. Grey matter and white matter tissues have approximately 4 ml (100 g)$^{-1}$ and 2 ml (100 g)$^{-1}$ of blood CBV value, respectively, which leads to a very high grey matter-white matter contrast in CBV maps. MTT is measured in units of seconds, while both grey matter and white matter tissue MTT values are approximately 4 seconds, though the latter may be slightly longer. That is why a MTT map has much lower grey matter-white matter contrast than that in a CBF or CBV map. This research has been built upon a wide literature on cerebral perfusion MRI methods [4,9–15]. However, we have focused on the studies that are highly innovative in CBF quantification [16, 17], benefiting from significant contributions to AIF measurement based on DSC-MRI. As already established in the literature [6,18], the accurate measurement of AIF is a critical step in perfusion imaging methods, including ASL, CT, PET, and DSC-MRI, which is the subject matter of this dissertation. The literature has accounted for various aspects of AIF, trying to find out where to measure it, which methods (manual, automatic, semi-automatic) to use in selecting it, and the sources of artefacts in CBF quantification. This research has similarly sought for ways of resolving issues related to sources of artefacts, such as bolus delay and dispersion effects, peak truncation effects, contrast agent non-linearity effects, scaling to absolute units, and partial volume effect (PVE).

1.2   An Overview of AIF

In this section, we aim to make an in-depth analysis of AIF, by discussing its significance for perfusion quantification and addressing the main methodological questions concerning AIF measurement.

1.2.1 Defining the Function

Perfusion imaging (DSC-MRI) starts with the injection of a paramagnetic contrast agent to a peripheral vein, and proceeds with the detection of the transient signal intensity change as the contrast agent arrives at the brain. The concentration of the contrast agent is determined based on the induced changes in relaxation rate. Early studies on DSC-MRI quantified the perfusion data through "summary parameters" [4]: the time-to-peak (TTP), the bolus arrival time (BAT), the maximum peak-concentration (MPC), the full-width at half-maximum (FWHM), or the first moment (FM) of the concentration time-course. It was later found out that these parameters depend on both tissue properties such as CBF and MTT and non-tissue related features (e.g. arterial status, cardiac output, injection rate, vascular path to the tissue). This implies that the physiological interpretation of the data acquired through DSC-MRI is a highly complicated task [19, 20]. To give an example for the complexity of the task, let us look at how the same concentration-time curve can be obtained in tissue regions (or in patients) with two very different perfusion conditions (Figure 1.1a) [18]. In the first case, a very fast and narrow bolus enters the tissue and leaves very slowly due to severe hypoperfusion and prolonged MTT. In the second case, a very slow and wide bolus enters the tissue, but this time leaves very fast due to hyperperfusion and reduced MTT. In spite of the very different tissue statuses (hypoperfusion and hyperperfusion, respectively), both these cases may lead to the same measured tissue concentration, and thus, the same summary parameter values.
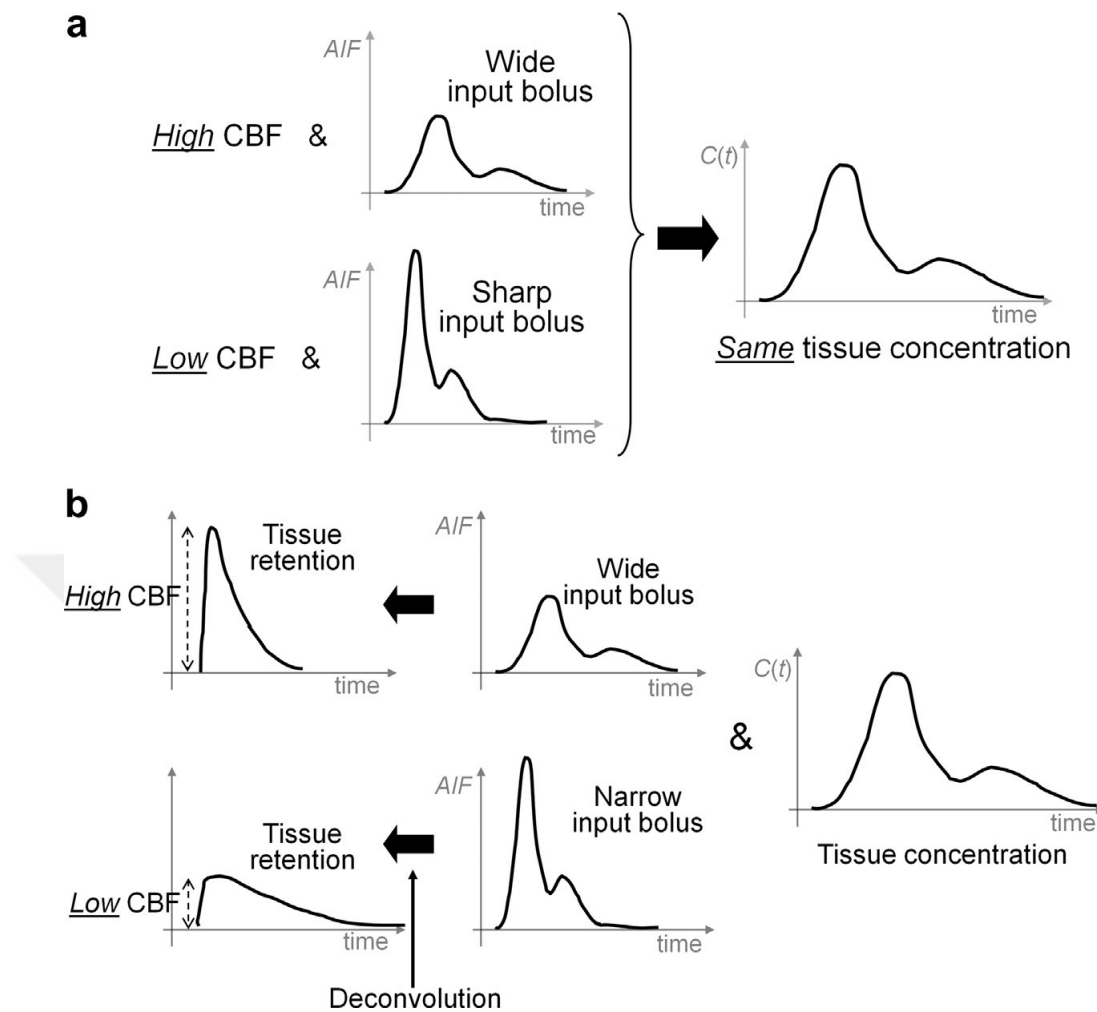
Figure 1.1 Illustration to explain the requirement for AIF measurement. a Two different bolus arrivals to the brain, and two different tissue CBF. In the first one bolus delivery is slow but the tissue has high CBF; in the second one bolus delivery is fast but the tissue has low CBF. It is impossible to differentiate the CBF in both cases using only the summary parameters since both cases result in the same tissue curve, C(t). b These two cases can be differentiated by using C(t) and AIF of each case and applying deconvolution analysis. For each case the tissue retention which is scaled by CBF is recovered. Thus two different CBF conditions are revealed [18].

Non-tissue related standards concerning the injection rate and the volume of contrast agent are known to be significant for controlling some of the factors that determine the shape of the tissue concentration curve. However, these standards have only a limited impact on the actual shape of the bolus entering the tissue. When a contrast agent is injected in a peripheral vein (e.g. the antecubital vein), it arrives at the brain only after traveling to the heart, then to the lungs, and back to the heart. In cases of arterial stenosis or collateral path due to an arterial occlusion, contrast agent travels through an alternative arterial pathway, which in turn distorts the bolus

shape on its way to the target tissue [21]. In numerical terms, 20 ml of contrast agent volume is injected with a power injector at a rate of 5ml s^{-1}, which results in a 4 s width of bolus at the injection site. However, the bolus is much wider (typically 20 s in width) when measured passing through the MCA in the brain. As the reader can guess, the injection rate changes the actual value of the AIF width and therefore plays a major role in CBF quantification. A study carried out with simulations using a human vasculature model demonstrated that injection speeds less than 3 ml s^{-1} result in the underestimation of CBF, and also, increasing the injection rate does not necessarily improve CBF estimations [22]. It was also argued that the AIF shape does not significantly change when the rate increases from 5 ml s^{-1} to 10 ml s^{-1}, a situation that is usually related to bolus dispersion through the heart-lungs-heart system. Based on these findings, we maintain that it is crucial to know how the contrast agent enters the tissue. This knowledge is essential to our ability to explain the confounding effects mentioned above and to distinguish the true microvascular (i.e. related to the tissue) information from the measured concentration-time curve (Figure 1.1b). This information itself constitutes the arterial input function, that is, the function indicating the time-dependent concentration input to the tissue [18].

1.2.2   Perfusion Quantification without an AIF

It is crucial to note here that we need to make a distinction between quantifying DSC-MRI data and quantifying perfusion using DSC-MRI data. We have already discussed above that DSC-MRI data can be quantified using only the "summary parameters", and without measuring an AIF. We have also implied that the relationship between any of these parameters and CBF is quite complicated, and, none of these parameters is reliable enough in calculating CBF [20]. This brings us to the necessity of AIF for quantifying perfusion. Finding AIF is essential to accurate CBF measurement, which in turn is indispensable to the diagnosis and treatment of certain brain pathologies. This is not to ignore the current debates about acute stroke imaging, with some studies arguing that one would yield the same results in infarct prediction by using only summary parameters (without an AIF) [18].

1.2.3   The AIF shape

Contrast agent is injected as a bolus in DSC-MRI studies. The transient change in signal intensity is mainly observed as a peak (first passage) with a wash-in (rise) and wash-out (fall) periods. The initial signals measured before the arrival of the bolus constitute the baseline. The first passage is followed by a smaller second peak which falls down towards baseline level. This segment is known as "recirculation", but the name can be misleading since the signal measured during this period is not related with the return of the contrast agent to the brain after the first passage. It originates from the injected bolus that was distributed to other organs mainly the thyroid, kidneys and lymph nodes [22]. Some studies have assumed the recirculation to be related to the first passage [23]. Most of the functions proposed for modeling the AIF concerns modeling the first passage of the bolus. These models are widely used, especially in numerical simulation studies to evaluate DSC-MRI analysis methods [6, 13, 20, 21, 24–30], or to remove the contributions from the contrast agent from recirculation while assessing in vivo data. Gamma-variate function can be considered as the most popular model [31,32]

$$AIF(t) = A(t - BAT)^b e^{-\frac{(t-BAT)}{C}} \tag{1.3}$$

In the function, A stands for scaling factor, while the shape of the peak is determined by B and C. BAT is the bolus arrival time.

1.2.4   AIF Measurement

This section aims to discuss the procedural details of AIF measurement, guided by the following questions: Why do we need to measure AIF? Where should we measure it? How do we know which curve is the best AIF candidate? Which criteria should be taken into account when evaluating the measured curves?

1.2.4.1   Where to Measure AIF.   As already indicated, AIF describes the time-dependent concentration input to the tissue. Regarding the complexity of the vascular structure of the brain, each region has a different blood supply. This implies that, for each voxel in the brain one should obtain a different AIF since the tissue at each brain location may have a different input shape of contrast agent [28]. If that is the case, one should measure the AIF from small arteries supplying blood to the tissue in a voxel (see Figure 1.2 for a demonstration of this measuring technique). There are, yet, certain problems that impede the AIF measurement from a small artery. Before all, the coarse spatial resolution of DSC-MRI, where a voxel size is usually $2 \times 2 \times 5 \text{ mm}^3$, makes it difficult to measure the signal from inside a small artery, as the latter is hardly distinguishable from the surrounding tissue. Here, we are talking about partial volume effect (PVE), which causes major errors in the measurement of AIF shape. Therefore to minimize PVE it would be wiser to measure AIF from a large artery (location 3 in Figure 1.2). However, large arteries are located distal to the tissue, which would result in altered shape of the bolus on its route to the tissue due to delay and dispersion. Obviously there is a trade off between measuring AIF on a small artery on the tissue proximity (for a correct input bolus shape) and measuring AIF on a large artery (for minimizing PVE) located far from the tissue (Figure 1.2).
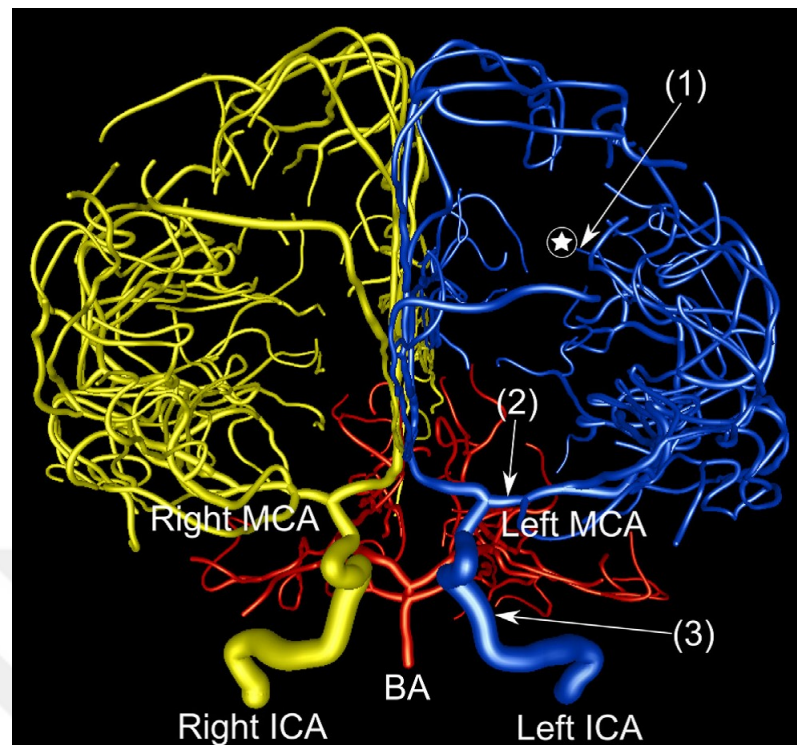
Figure 1.2 Cerebral arteries (MCA: middle cerebral artery, ICA: internal carotid artery, BA: basilar artery) and the location alternatives for AIF measurement. The vascular territories of the right ICA, left ICA and BA are labelled with green, blue, and red colours, respectively. If we want to calculate cerebral blood flow (CBF) in a tissue voxel located in the position labelled by the star symbol, the AIF should ideally be measured from the signal changes in the small arteriole supplying the tissue in that voxel (location labelled (1) in the figure). Since the small size of this arteriole is a potential reason for partial volume effect, a larger artery (ICA in location (3)) would be a better location to measure the AIF. However, ICA is remote from the tissue of interest, which is disadvantageous for it may cause bolus delay and dispersion. For this reason M1 segment of the MCA (location (2)) is usually preferred when measuring the AIF, given that it is relatively closer to the tissue compared to ICA [18].

1.2.4.2   Local / Global AIF.   There seems to be two options for measuring AIF. We will either measure it in a small artery to better estimate the bolus, or prefer a large artery distal to the tissue of interest to avoid complications caused by PVE. However, either option is far away from being the perfect solution, and one should rather make case-based decisions. In some cases (for example, in severe cerebrovascular diseases such as the moyamoya syndrome) it can be wiser to measure the AIF from a small proximal artery, compromising to some extent on PVE [33, 34]. In other cases (e.g. epilepsy, multiple sclerosis), where arterial abnormalities are out of question, AIF should be measured from a large artery, such as the M1 segment of the MCA. This way, the researcher would both minimize the risk of PVE and avoid AIF shape distortions due

to the effects of bolus delay and dispersion [18]. The literature has introduced the concepts of global AIF and local AIF as a terminology for AIF measurement in large and small arterial locations. DSC-MRI studies have mostly used a single measurement of AIF from a large artery as an input for the tissue in the whole brain to evaluate perfusion. DSC-MRI analysis tools (manual or automatic) are designed to find this global AIF. On the other hand, AIF can also be measured from a small artery, and yet this also raises two choices. One is to use this AIF as an input for all the brain tissue, considering it as a global AIF. The other choice is to use the AIF as an input only for the tissue supplied by that small artery, considering it as a local AIF. In the latter case, several AIFs are measured to be inputs for other tissue regions. If an AIF is assigned for major arterial territories (MCA, posterior cerebral artery) then local AIF is referred to as regional AIF. Researchers have developed several local and regional AIF methods [23, 35–41] since it was first introduced by Calamante et al. [42] in 2004. The aim of using local AIFs is to minimize the CBF quantification errors related with bolus dispersion. However, local AIF methods are still not widely implemented, as they are not found to be truly valid [39, 43]. Local AIF software tools to be developed by scanner manufacturers are believed to improve this method. Apart from the issue of remoteness from the tissue of interest, global AIF measurement can be problematic due to the inevitable drop of signal to noise level at the peak of the bolus. This complete signal loss is related to dephasing induced by the contrast agent. AIF is usually measured from the M1 segment of the MCA by the DSC-MRI studies at 1.5 T [6]. The M1 segment is considered advantageous since it is not too far away from the tissue (location (2) in Figure 1.2) and has a fairly large diameter that reduces the risk of PVE to some extent. However, at 3T, the complete dephasing of the signal occurs (at typical TE values in single echo gradient echo EPI sequences) in the M1 segment of the MCA, and this condition leads to the underestimation of the peak. To avoid this signal truncation effect, AIF should be measured in the M2 or M3 segments of the MCA, but doing so, one takes the increased risk of PVE at the same time. In their perfusion study on stroke patients, Ebinger et al. [44] found that AIF selection at the MCA has a major impact on CBF quantification, and suggested to use the distal branch of the MCA (e.g. M3), contralateral to the ischaemic lesion. Another option is to measure AIF from completely outside the M1 segment of the MCA (suggested

locations relative to the location of the artery are explained in Section 1.3), which, in spite of the PVE, can result in acceptable approximation of the curve shape.

1.2.4.3 Inside / Outside the Artery.   AIF, as the name implies, should be measured from inside an artery or from a partial volume voxel where the arterial signal is dominant over tissue signal. However, there are many studies that measure AIF outside the artery [45]. In manual AIF selection, some DSC-MRI users are not doing this on purpose, as they select the AIF voxels by evaluating the bolus curves regarding the characteristics such as peak height, full width half maximum, arrival time and area under curve, etc. in a region around an artery. The criteria sought for the AIF characteristics are high and narrow peak and early arrival time. Exclusively relying on these criteria, the user usually doesn't check the location of the selected voxels relative to the position of the artery.

Decision on the location of AIF measurement (from inside or outside the artery) is related with the type of the sequence being used. The susceptibility effect of the contrast agent relative to the vessel size is different for gradient-echo and spin-echo based sequences [46, 47]. Spin-echo based sequences are responsive to small vessel size, while gradient-echo sequences are sensitive to all sizes [48]. If we take into account this increased sensitivity to large vessels in gradient-echo sequences, together with the high concentration of the contrast agent inside the artery, it turns out to be highly difficult to measure an AIF in good shape using DSC-MRI data with typical TE values (TE = 35-45 ms at 1.5 T, or 25-30 ms at 3 T for gradient-echo EPI [49]). At these TE values, with the passage of the bolus, complete signal dephasing causes the signal inside the artery to reach at the noise level (Figure 1.3).
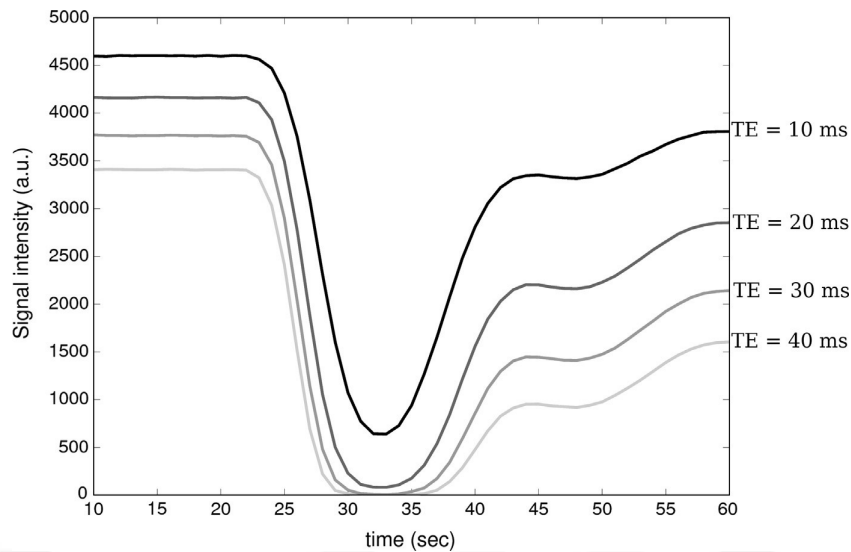
Figure 1.3 Simulated AIF measurement inside an artery using a single-echo gradient-echo esquence. AIFs were taken from a vascular model at [22] for a typical dose of contrast agent. During the bolus passage, the complete signal dephasing is observed for TEs longer than approximately 20 ms which resulted in truncation of the AIF shape [18].

To avoid the signal truncation at the peak of the bolus, a very short TE should be used, which is possible only when multi-echo sequences are used. Otherwise, AIF is usually measured from tissue outside the artery in gradient-echo based sequences.

1.2.4.4   Manual and Automatic Methods.   The existing literature has so far applied different manual [50] and automatic AIF selection methods [51–56]. The manual method entails search in the arterial region (e.g. MCA) for concentration time curves (CTCs) that have early, high and narrow peaks. The users select a region-of-interest (ROI) and, considering the overall characteristics of the bolus passage, determines the mean curve of the voxels in this ROI as the global AIF. In DSC-MRI studies, factors such as the injection technique, cardiac output, and vascular condition differ across patients, which is why the measured bolus may not be equally sharp and narrow for every patient. During trials, the users make comparisons of concentration time curves, and, when they find a peak that is narrower, taller and has an earlier arrival time, they decide to use it as the AIF. It is very likely that different users would decide on different AIFs during evaluation. Thus, obviously, the downside of the manual method is that it is highly subjective, time consuming and prone to inconsistencies in

determining arterial voxels [51–54]. Several fully and semi-automatic methods were developed to overcome these shortcomings [51–54]. Automatic methods employ a search algorithm to identify the voxels that meet certain ad hoc criteria related to the features of the concentration time course. These criteria include high peak height (PH), small full-width-at-half-maximum (FWHM), early time-to-peak (TTP), and early arrival time (AT) [51–55]. The automatic methods are faster, more reproducible and objective than the manual selection. They can widely be used in hospitals by the staff with limited expertise. However, they are used as a "black box", since the user has almost no control on the output of the searching algorithm. Automatic AIF selection is usually integrated to an automatic DSC-MRI analysis software [55–57], where the deconvolution analysis is also automatically performed and the user is provided only with the final perfusion maps. We agree that automatic DSC-MRI methods may introduce errors, no matter how sophisticated the AIF searching algorithms may be. To increase the reliability of the procedure, the user should have the means to intervene during the analysis where possible [58]. Specifically, the user should be able to observe both the spatial location of the selected voxels relative to the artery and the shape of the concentration time curve (whether the curve is distorted or not) prior to accepting it as the AIF. To sum up, the use of automatic AIF searching methods is highly recommended to improve objectivity and reliability. However, user control should be available so that the perfusion evaluation can be accomplished deliberately.

1.3   The Aim of the Study

In the above section, we have noted that the literature has developed the following criteria for selecting AIF: high peak height (PH), small full-width-at-half-maximum (FWHM), early time-to-peak (TTP), and early arrival time (AT). However, it has been found that high PH and small FWHM may indicate a shape distortion due to PVE [59]. Therefore, the concentration time curves (CTCs) labeled as AIF by the automatic selection method are at times questionable since the PVE factor is disregarded. In an effort to resolve the PVE problem, Bleeker et al. [16] introduced a new parameter, the SS:AUC ratio, that is defined as the ratio of the mean steady state (SS) value (post-

bolus equilibrium) to the area under the curve (AUC) of the first passage of contrast agent. The reference value for the SS:AUC ratio was obtained from the tissue, where there is linearity between the change of the transverse relaxation rate (ΔR2*) and the concentration of the contrast agent. This reference value was used for picking out the CTCs that were not distorted by PVE. By employing the SS:AUC ratio, Bleeker et al. [16] evaluated the CTCs in and around the middle cerebral artery (MCA), and concluded that measurements within and anterior to the MCA show PVEs because the magnetic field inside and outside the vessel changes due to contrast agent, affecting in turn the gradient echo MR signal outside the vessel.

The CTCs corrupted by PVE demonstrate three types of shape characteristics [16]. In the first type, the CTCs have higher peaks and smaller FWHMs than the true reference. In the second type, two peaks are observed in the first passage of the contrast agent. In the third type, no first pass peak is detected while high SS amplitude is observed. It was also demonstrated (by simulations and in vivo) that, in general, AIF is better if measured in tissue located outside the MCA rather than in voxels on the artery. The possible locations for AIF might differ across patients as the angle between the vessel and the main magnetic field deviates from 90deg. However, the AIF is usually found to be free of PVE when the voxels are superior and posterior to the MCA [16].

As implied in earlier research, the parametric evaluation of CTCs does not guarantee correct AIF measurements, and the knowledge of spatial location of the AIF voxel is highly crucial for the procedure [18]. In this study we aim to improve AIF selection by utilizing magnetic resonance angiography (MRA) as a tool for identifying arterial locations during the parametric evaluation of CTCs, and thereby resolving problems that usually lead to shape distortions in AIF.

As we carried out our research, we explored the utility of both manual and automatic/semi-automatic AIF selection methods. The semi-automatic AIF selection method is based on the cluster analysis of the CTC parameters (FWHM, PH, AT, TTP, SS, AUC, SS:AUC) obtained from the voxels located within and around the MCA.

2. MATERIALS AND METHODS

2.1 Patients

We worked on the MR images of six patients with brain tumors, who had already been scheduled for perfusion imaging. Informed consent was obtained from all individual participants included in the study for anonymized use of their MR images. The study was approved by the local institutional review board.

2.2 Magnetic Resonance Imaging

The MR images were acquired by a 3T MR system (Achieva, Philips Medical Systems) using the 8 channel sense head coil.

For perfusion imaging, a transverse T2*-weighted pulse sequence with three dimensional (3D) echo-planar principles of echo shifting with a train of observations (PRESTO) was used [60]. The parameters are TR (repetition time) = 16 ms; TE (echo time) = 24 ms; flip angle = 7 deg; data matrix = 144 × 144; slice thickness = 4 mm with 30 slices per single slab; voxel resolution of 1.67 × 1.67 × 4 mm; field of view = 240 mm. Patients received 0.1 mmol/kg body weight of a contrast agent Gd-DTPA (Magnevist, Bayer Schering Pharma AG, Leverkusen, Germany). The contrast agent was injected using a power injector at a rate of 5 ml/s, followed by a 20 ml saline flush at the same injection rate.

The MRA images were acquired with a 3D time-of-flight (TOF) sequence (TR = 25 ms; TE = 3.5 ms; SENSE = 2.0; voxel resolution of 0.375 × 0.375 × 4 mm).

T2-weighted images were acquired with SPIR sequence (TR = 3000 ms; TE = 80 ms; flip angle = 90 deg; data matrix = 560 × 560; slice thickness = 4 mm with 30

slices per single slab; voxel resolution of $0.4464 \times 0.4464 \times 4$ mm).

2.3 Image Registration

Perfusion images were co-registered with the MRA images employing SPM8 (Wellcome Trust Centre for Neuroimaging, Institute of Neurology, UCL, London UK-http://www.fil.ion.ucl.ac.uk/spm). For each perfusion image slice, the mean image of the time series (i.e. 60 dynamic scans) was calculated and used for registering to the MRA images. 5 images of the time series of a perfusion scan were shown in Figure 2.1.
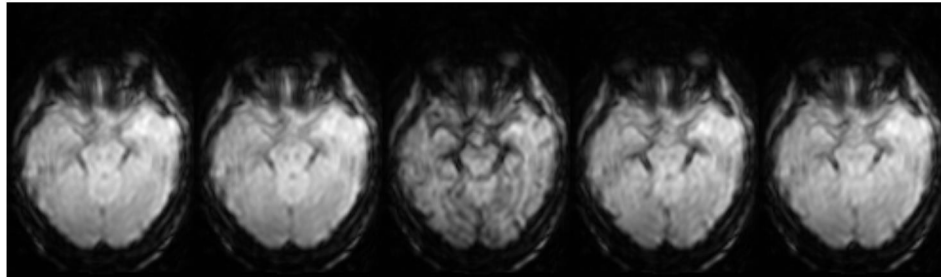
Figure 2.1 Five images of the time series of perfusion imaging. From left to right; images are from baseline, contrast arrival (wash in), peak contrast, contrast removal (wash out) and steady state periods.

The transformation matrix of this registration was applied on to all time frames of the perfusion scan. Normalized mutual information was used as the objective function in the estimation options and trilinear interpolation was applied to reslice perfusion images. Finally, T2-weighted images were registered to the MRA images. Samples of MRA and T2-weighted images are shown in Figure 2.2.
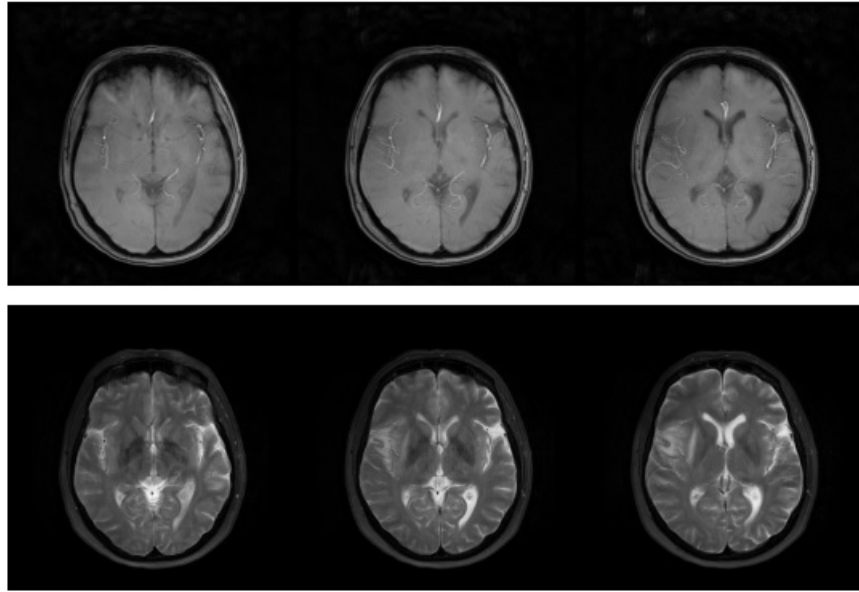
Figure 2.2 MRA (top row) and T2-weighted (bottom row) images of 3 slices.

After image registration, we wanted to monitor the first pass of the contrast agent through the cerebral arteries. To visualize the arteries, we created perfusion movies by overlaying the MRA images on top of the perfusion image series. The snapshots of the movies of the slices containing the MCA are shown in Figure 2.3. Red arrows point at the signal intensity drop that occurs as the contrast matter arrives at the MCA.
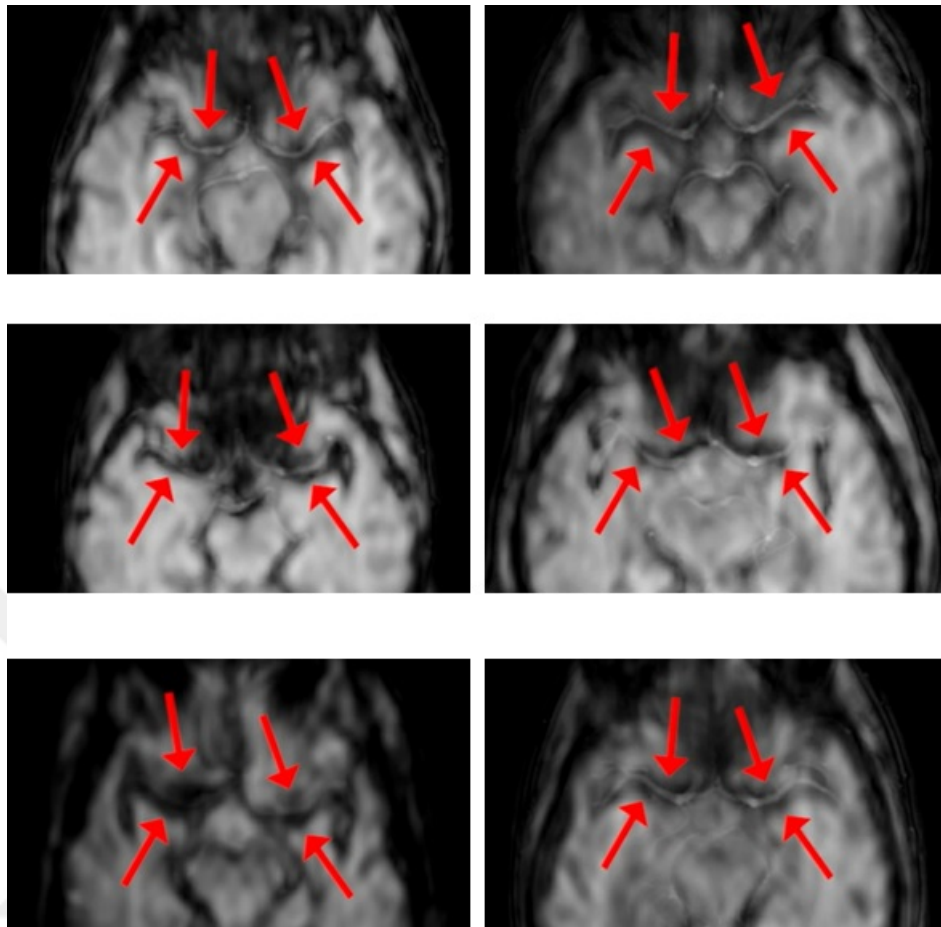
Figure 2.3 The snapshots of the movies of the slices containing the MCA. Red arrows point at the signal intensity drop that occurs as the contrast matter arrives at the MCA.

2.4 MCA Segmentation

All image processing in the rest of the study was carried out by using in-house Matlab (R2013b, the MathWorks Inc, Natick, MA, USA) code. For each patient, we selected TOF MRA image slices where the M1 segment of MCA was visible, and defined a region-of-interest (ROI) that contains the artery (ROI 1 for the right and ROI 2 for the left hemisphere, see Figure 2.4). Arterial voxels in each ROI were segmented by simple intensity thresholding.
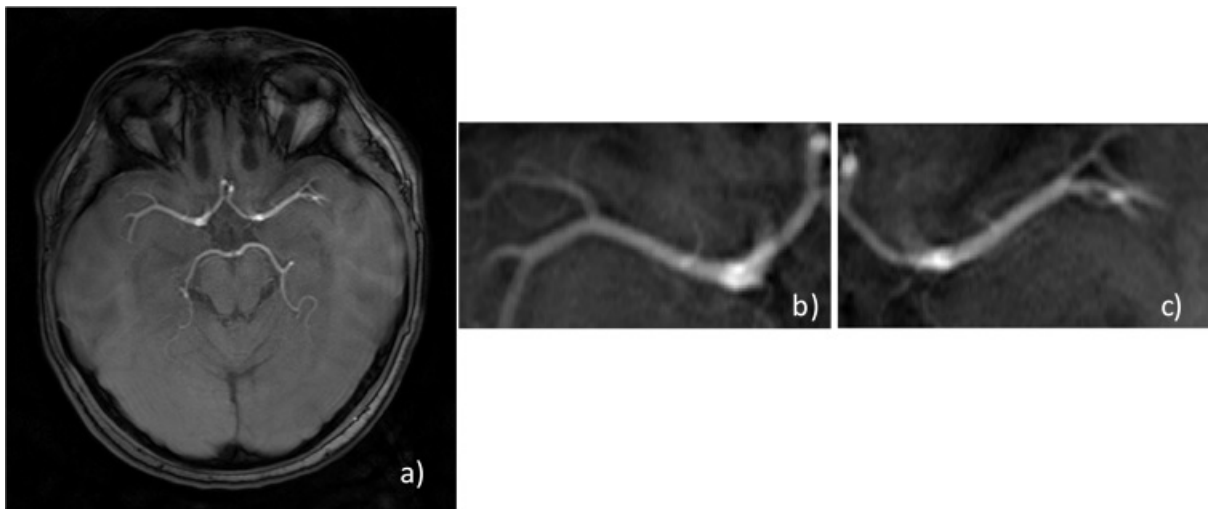
Figure 2.4 **a)** MRA image of the MCA, **b)** ROI 1 for the right hemisphere, **c)** ROI 2 for the left hemisphere.

2.5   Dilation of MCA

Segmented MCA was expanded through 3D image dilation. Each branch was dilated in all directions with a pyramid shaped structuring element in order to encapsulate the MCA as illustrated in Figure 2.5a and Figure 2.5b. This dilated volume contains voxels that are located both inside and outside the artery.
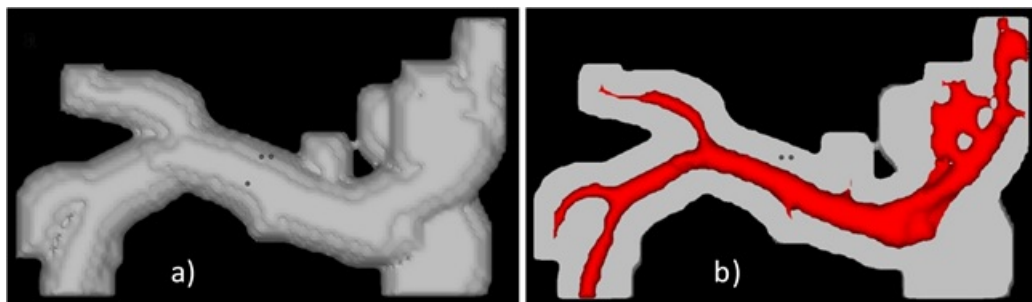
Figure 2.5 3D volume rendering of middle cerebral artery. **a)** The volume computed by the 3D image dilation of the segmented MCA, **b)** the coronal cross section of the volume that encapsulates the MCA.

2.6 CTC Parameters

For each voxel in the dilated volume, we computed the CTC parameters (PH, FWHM, TTP, AT, SS, AUC, SS:AUC ratio) that have been widely used for AIF selection [51–56] (Figure 2.6). The dilated volume covers three brain slices: the slice including the MCA, and the slices that are inferior and posterior to the MCA.
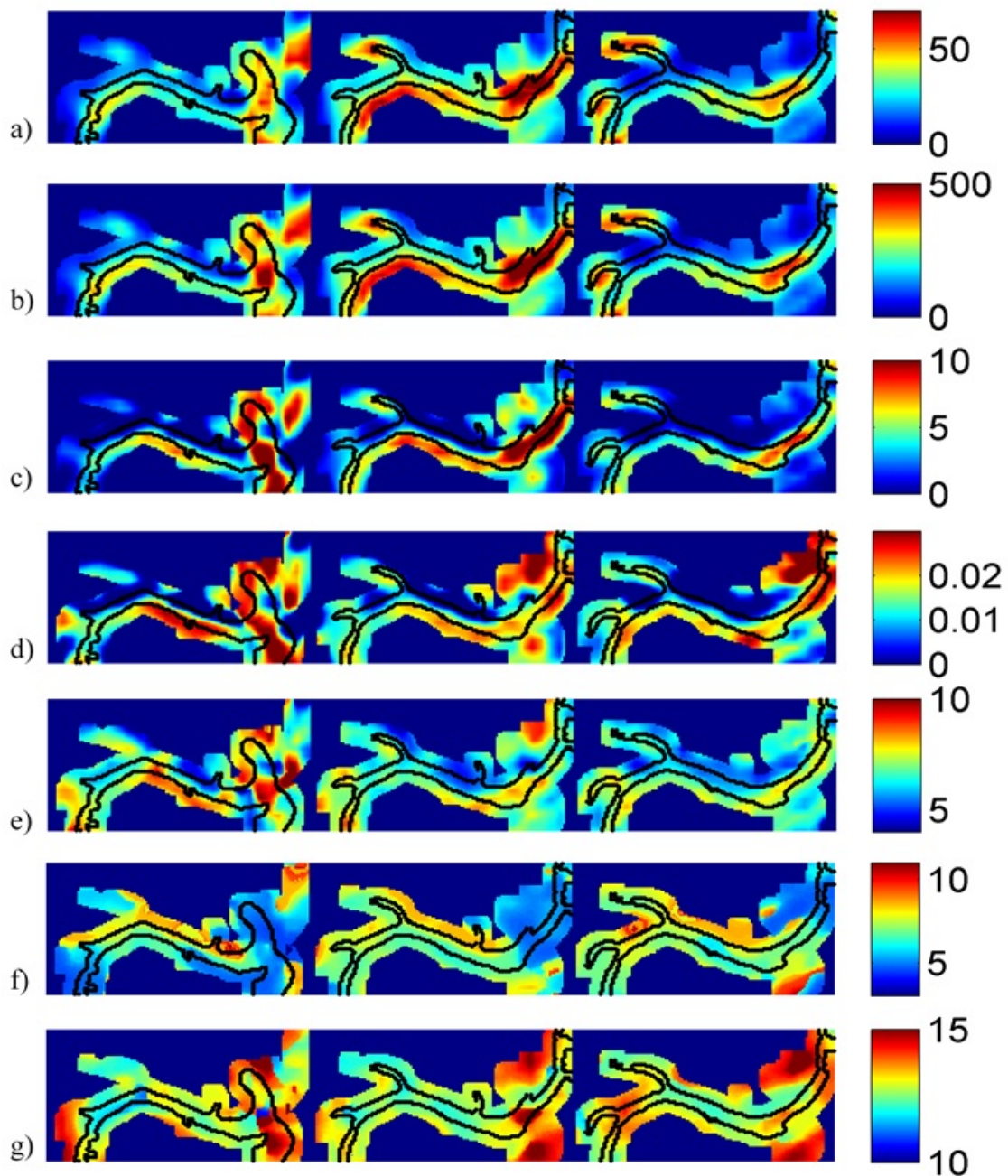
Figure 2.6 CTC parameters (arbitrary units). **a)** PH, **b)** AUC, **c)** SS, **d)** SS:AUC, **e)** FWHM, **f)** AT, **g)** TTP of three successive slices (Left: Inferior slice, Middle: MCA slice, Right: Superior slice) of the dilated volume

2.7   AIF Selection Methods

In this study we examined the utility of both manual and automatic/semi-automatic AIF selection methods. We explain below the procedures for the particular techniques we have tried out. We aimed to improve each selection technique by utilizing MRA as a tool for identifying arterial locations during parametric evaluation of CTCs. In both methods, we worked on the CTC parameters (FWHM, PH, AT, TTP, SS, AUC, SS:AUC) obtained from the voxels located within and around the MCA. We calculated SS:AUC from venous output function (VOF) which is obtained from the superior sagittal sinus and used it as a reference in selecting AIF.

2.7.1   Manual AIF Selection

A user interface was designed in MATLAB for determining the CTCs that show AIF characteristics.

To filter out CTCs, the ad hoc criteria suggested in literature (relatively high PH, AUC and SS values, and relatively low AT, TTP, FWHM values) were experimented through this interface.

We set thresholds on the parameters by trial and error, and observed the pixels corresponding these CTCs on the MRA image. The screenshots of the interface for ROI1 and ROI2 are shown in Figure 2.7a and Figure 2.7b, respectively.
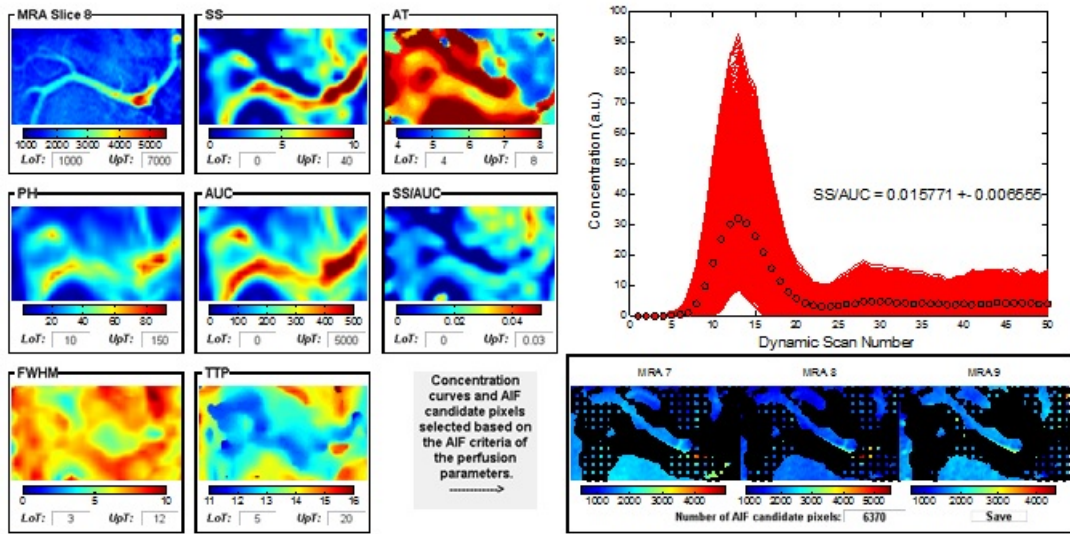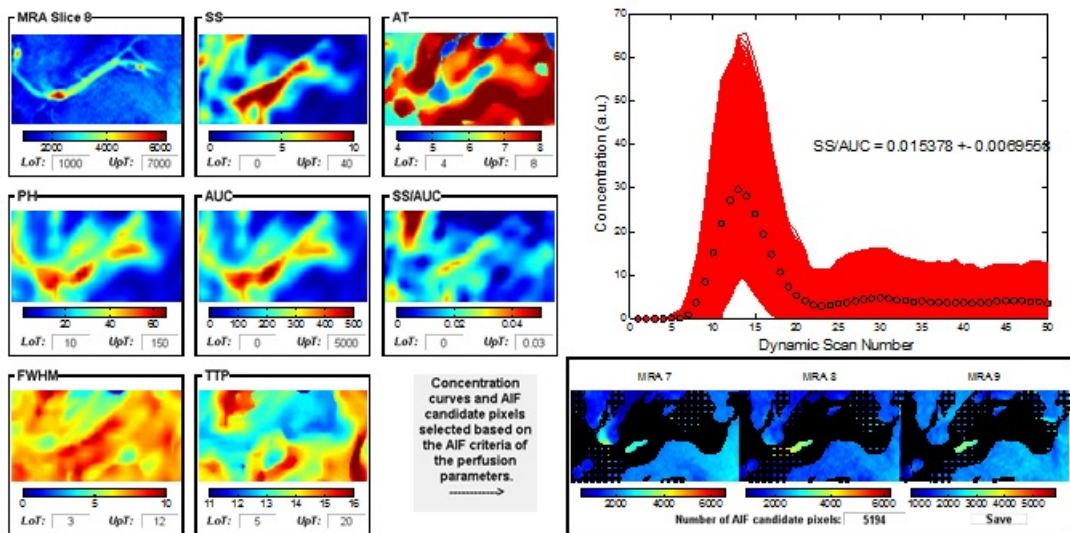
Figure 2.7 Interface for manual AIF selection. The screenshots of the interface **a)** for ROI1 and **b)** for ROI2.

The interface is composed of three sections. Eight frames are displayed in the first section (left column), each including a parametric image, a colorbar that indicates the range of values from minumum (blue) to maximum (red), and two edit boxes for setting lower and upper thresholds. The second section (middle column) presents the CTCs of which parameters fall between the lower and upper thresholds. The third section (right column) shows the spatial locations (black dots) of the voxels from which

the CTCs were obtained.

The interface enables the user to set a lower and upper threshold for each parameter, thus to select the CTCs with parameters that fall between these thresholds, and to observe the voxel locations of these CTCs on the MRA image of the ROI.

2.7.1.1   Parameter Thresholds and Locating Voxels on MRA Images.   Interface initially takes all CTC parameters between the lowest and highest threshold values in order to consider all concentration changes as potential candidates for AIF (see the left columns of Figure 2.7a and Figure 2.7b). Next, the user experiments with the parameter thresholds to see how the CTCs and the related voxel locations change across different threshold values. At each threshold setting, the mean and the standard deviation of all parameters are observed so that the user can finally obtain CTCs with common shape characteristics. The time average of these CTCs is set as the AIF (the black circles in the middle column of Figure 2.7a and Figure 2.7b). During threshold settings the interface also helps locate on MRA images the voxels corresponding to the CTCs (see the right columns of Figure 2.7a and Figure 2.7b). The use of the interface for AIF selection is demonstrated with an example in the results section.

The interface can also be used to detect shape distorted CTCs by setting thresholds outside the acceptable range of the SS:AUC parameter. Examples are provided in the results section.

As our research has confirmed, the manual AIF selection techniques have certain disadvantages. They are highly subjective, time consuming and prone to inconsistencies in determining AIF. Therefore, we employed a semi-automatic method in our study to overcome these shortcomings. The major contributions of this research are based on this method, which is outlined in the following sections.

2.7.2   Semi-automatic Method

Our semi-automatic AIF selection method is based on the cluster analysis of the CTC parameters obtained from the voxels located within and around the MCA. At the onset of the study, a binary MCA image obtained through MRA is dilated so as to observe all voxels within and around the MCA (anterior, posterior, superior, and inferior). The CTC parameters of these voxels are computed, to be used as inputs to a fuzzy clustering algorithm. Clusters are then classified by way of parametric evaluation, which guides us in detecting both the AIF voxel and shape distortions due to PVE. As we evaluate the clusters, we treat SS:AUC as the most important parameter that is decisive in detecting PVE. In the last stage of the study, we carry out angiographic investigation for comparatively examining the clusters exhibiting AIF characteristics and those containing distorted CTCs due to PVE.

2.7.2.1   The Method of Cluster Analysis.   Since the range of CTC parameter values of AIF are not known a priori, it is hard to identify AIF based on an absolute threshold level.

In this study, we employed the fuzzy c-means clustering technique in MATLAB to divide the CTCs into groups with similar parameter values for each voxel within the dilated volume [52,54]. Prior to clustering, all parameters were rescaled to a range of 0 to 1 so that none of them would dominate when calculating the distances throughout clustering.

Since the employed clustering technique is unsupervised, the possible number of classes is as many as the number of voxels. To arrive at a reasonable number of clusters we employed a method that looks at the percentage of variation explained (POVE), which is the ratio of between-group variance ($\sigma^2_{between}$) to the total variance (σ^2_{total}) as explained in Equations 2-4. When POVE is plotted as a function of the number of clusters, a breaking point is observed with diminishing marginal gain as the number of clusters increased. Figure 2.8 demonstrates the POVE vs number of clusters.
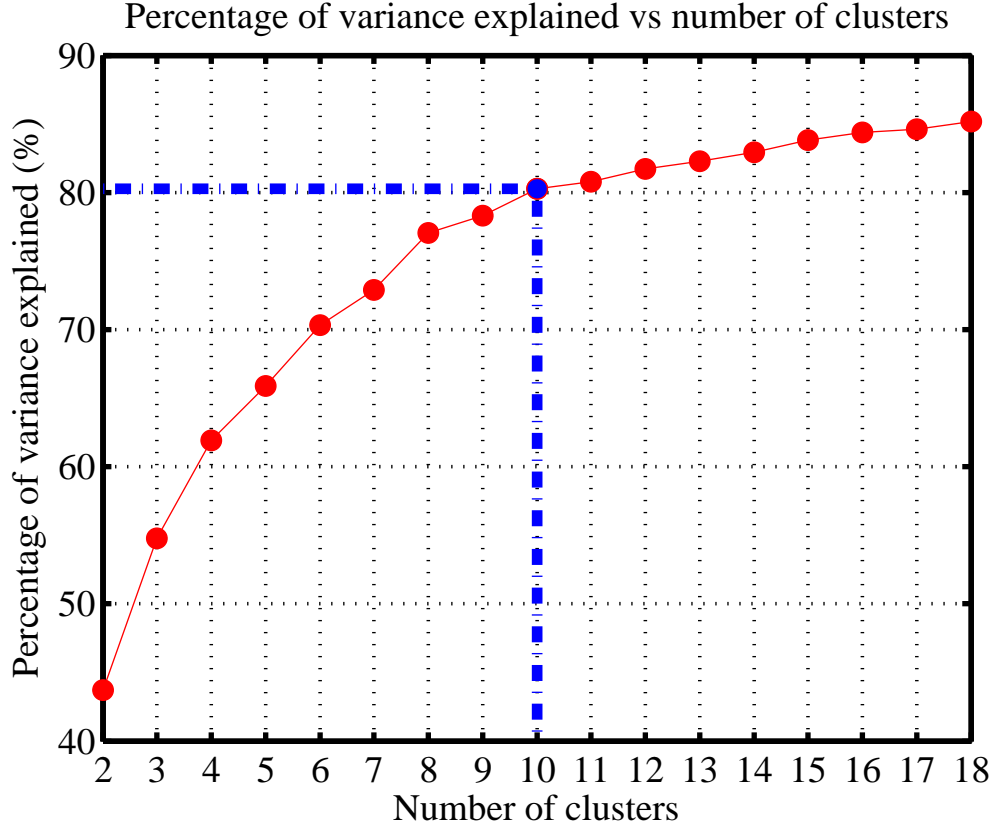
Figure 2.8 POVE vs number of clusters.

$$\sigma^2_{between} = \sum_j n_j (\bar{y}_j - \bar{y})^2 \tag{2.1}$$

$$\sigma^2_{total} = \sum_j \sum_i (\bar{y}_{ij} - \bar{y})^2 \tag{2.2}$$

$$POVE = \frac{\sigma^2_{between}}{\sigma^2_{total}} \tag{2.3}$$

where n_j is the number of elements in group j, $\bar{y}_j$ is the mean of group j and $\bar{y}$ is the mean of all samples.

Therefore, decision on the number of clusters is contingent on the significance

of a change in POVE. In our study, we stopped increasing the number of clusters when the marginal gain was less than 1% (Figure 2.8). Once the number of clusters was decided, each clustering was repeated 10 times to assure that the initialization did not make any difference in the clusters. Thereby the reproducibility of the results was ensured.

2.7.2.2 The Prevention of Shape Distortions in CTCs.   With the MRA images at hand, we were able to distinguish the arterial voxels from tissues in all clusters. This enabled us to prevent shape distortions in CTCs in two steps: (1) cluster modification by removing arterial voxels, and (2) AIF correction using venous output function (VOF).

In the first step, we removed arterial voxels when found in a cluster in order to prevent shape distortions in CTCs that might be caused by arterial signal saturation at peak concentration, arterial signal relocation during the passage of the contrast agent, and the non-linearity in $\Delta R2^*$ vs contrast in whole blood. To reveal the effect of removing arterial voxels, we compared the mean CTCs of the cluster before and after modification. The results of the comparisons are demonstrated in Section 3.1.

In the second step, aiming at correcting PVE, we rescaled the mean CTCs of the clusters (both before and after the modification) so that they will have the same AUC with that of the VOF, which is obtained from the superior sagittal sinus. Based on a correction factor ($\text{AUC}_{\text{VOF}}/\text{AUC}_{\text{CTC}}$), we tried to equalize the arterial time integral to the venous time integral. The advantage of using sagittal sinus for VOF is that PVE is already minimized in this vessel, since it has a large diameter and is almost perpendicular to several slices [61].

This step was also applied in unmodified clusters that already do not contain arterial voxels.

2.7.2.3 Defining AIFs with respect to SS:AUC. After minimizing the risk of shape distortion, we calculated SS:AUC of VOF and used it as a reference in selecting AIF among the rescaled mean CTCs (see Section 3.3). The mean CTC of the cluster that is close to the reference SS:AUC gives the selected AIF (AIF_S), whereas the one that is far from the reference value will be referred to as the eliminated AIF (AIF_E). If multiple clusters are close to the reference SS:AUC, the one with the highest AUC was labelled as AIF_S. Also note that AIF_E was selected among the mean CTCs of the clusters that is far from the reference SS:AUC but do not exhibit any shape distortions. The shape of AIF_E was visually assessed. This procedure was implemented in both ROI1 and ROI2.

2.7.2.4 Evaluating the clusters. Prior to rescaling the mean CTCs, all the clusters were re-numbered in an ascending order, starting from the lowest to the highest AUC. Next an image was generated where the clustered voxels were marked in a color scale from blue to red (blue for the cluster with the lowest AUC, red for the cluster with the highest AUC). The artery borders (the MCA edge) were imposed on the images in order to investigate AIF_S and AIF_E based on their locations with regard to the MCA (Figure 2.9).
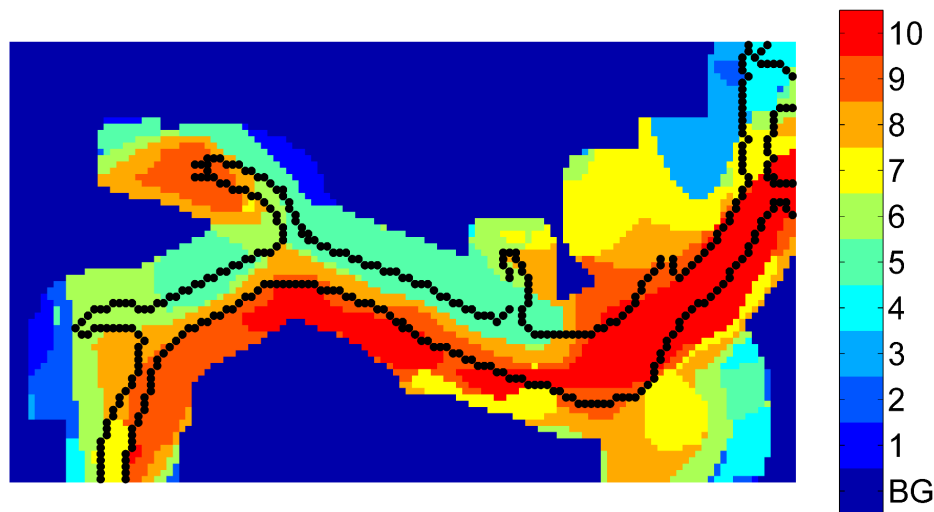
Figure 2.9 The MCA edge imposed on the cluster image (Colorbar indicates the background (BG) and cluster numbers. Blue and red designate the clusters with the lowest and highest AUCs, respectively).

2.7.2.5   Finding the CBF differences between AIF$_S$ and AIF$_E$.   Tissue-specific (GM) CBF maps ($CBF(AIF_S)$ and $CBF(AIF_E)$) were computed for all brain slices using AIF_S and AIF_E to compare the two AIFs in terms of the CBF values they result in. Differences in CBF values were calculated as follows:

$$CBF_{DIFF} = \frac{CBF(AIF_S) - CBF(AIF_E)}{CBF(AIF_S)} \tag{2.4}$$

To avoid errors caused by bolus delay, all the CTCs have been shifted to a common time origin before the deconvolution analysis has been performed. CBF calculations were carried out through Tikhonov regularization [35, 62]. This technique was utilized in estimating the impulse response whose initial value was recorded as the CBF value of a tissue voxel. The regularization parameter was selected according to the L-curve criterion [63], where the residual norm and the solution norm are kept reasonably small. To compute CBF differences (CBF_{DIFF}), we used GM voxels, as they allow for more practical image segmentation compared to tumors and provide sufficient data to perform descriptive statistics.

3. RESULTS

3.1 The results of manual AIF selection

3.1.1 Using the Interface for AIF Selection: Setting Thresholds on CTC Parameters

Figure 3.1 demonstrates how the CTCs and the related voxel locations change as the interface user experiments with the parameter thresholds (steps 1 to 4). The parameters used in this example (Patient 5) are the SS:AUC ratio and the PH. SS:AUC is the PVE related parameter whereas PH is the conventional AIF selecting parameter, which should be chosen at moderate levels since the highest peaks may indicate PVE.
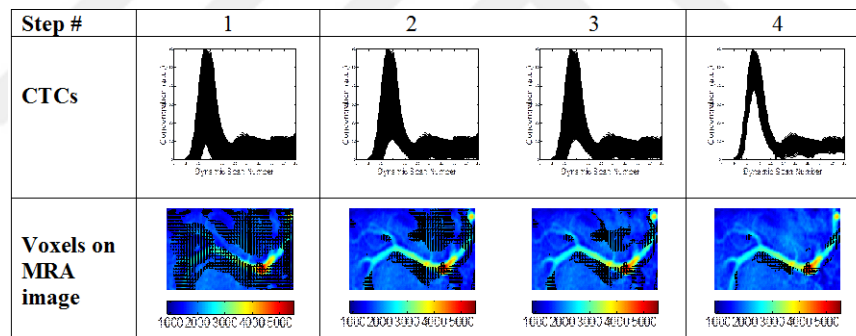
Figure 3.1 Filtering out CTCs by threshold setting. **a)** Remaining CTCs after threshold setting (see Table 3.1), **b)** Voxels on the MRA image.

The optimal number of CTCs is determined in four steps. The number of CTCs decreases as the range of lower and upper thresholds narrows down from 0-0.03 to 0.016-0.023 for the SS:AUC ratio and from 10-60 to 40-60 for the PH (Table 3.1).

In this example, the number of CTCs with common shape characteristics is 660 and the time avarage of these CTCs is set as the AIF.

For every threshold setting, the interface computes the mean and SD of all

Table 3.1
Number of CTCs after threshold setting.

Step #	1	2	3	4
Number of CTCs	6054	2907	2021	660
SS:AUC LoT	0	0.016	0.016	0.016
SS:AUC UpT	0.03	0.03	0.023	0.023
PH LoT	10	10	10	40
PH UpT	60	60	60	60

parameters of the remaining CTCs (Table 3.2). In this way, the user is able to decide whether or not to change the threshold values of other parameters.

A significant aspect of this AIF selection process is that one can start with the thresholds of any parameter and change those of others when needed. The purpose here is to decrease SD of all parameters of the remaining CTCs and obtain curves with common shape characteristics in terms of all parameters.

For the case demonstrated above, Table 3.2 demonstrates how the mean and the SD of FWHM, PH, and SS:AUC change at each step of threshold setting for SS:AUC ratio and PH.

3.1.2   Using the Interface for Detecting Shape Distortions

Using the interface we evaluated the MCA neighborhood with respect to PVE and came across the three types of shape distortions mentioned by Bleeker et al. [16]. Figure 3.2 exemplifies the first type, where CTCs with high peaks and small FWHMs were derived from the voxels located on and anterior to the MCA, which resulted in low SS:AUC ratios as shown in Table 3.3.

Table 3.2
The mean and the SD of FWHM, PH, and SS:AUC change at each step of threshold setting.

Step #	1	2	3	4
FWHM mean	6.922	7.278	7.119	7.048
FWHM SD	0.775	0.666	0.64	0.576
SD/mean (%)	11.20	9.15	8.99	8.17
SS:AUC ratio mean	0.016	0.021	0.019	0.019
SS:AUC ratio SD	0.007	0.004	0.002	0.002
SD/mean (%)	42.04	16.43	9.84	9.79
PH mean	31.3	31.88	35.48	48.24
PH SD	12	12.56	11.49	5.203
SD/mean (%)	38.34	39.41	32.39	10.79
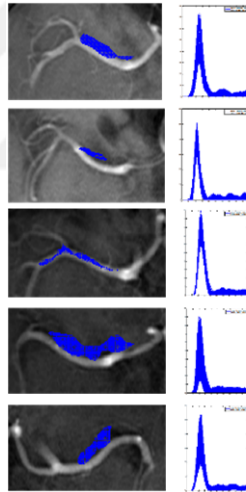
Figure 3.2 CTCs with high peaks and small FWHMs; and their locations (on and anterior to the MCA).

Table 3.3

Low SS:AUC ratios of the CTCs derived from voxels located on and anterior to the MCA.

PAT #	SS:AUC Mean	SS:AUC SD
Pat 6 (ROI1)	0.0056	0.0023
Pat 4 (ROI1)	0.0057	0.0046
Pat 2 (ROI1)	0.0059	0.0033
Pat 5 (ROI1)	0.0052	0.0034
Pat 5 (ROI2)	0.0068	0.0022

3.2   Results of Semi-automatic AIF Selection

3.2.1   Shape Distortions in CTCs

Comparisons of the clusters before and after modification (i.e. before and after removing the arterial voxels) reveal significant differences in the mean CTCs, as shown in Figure 3.3. The SS:AUC ratio of the mean CTC in modified clusters got closer to the reference SS:AUC.
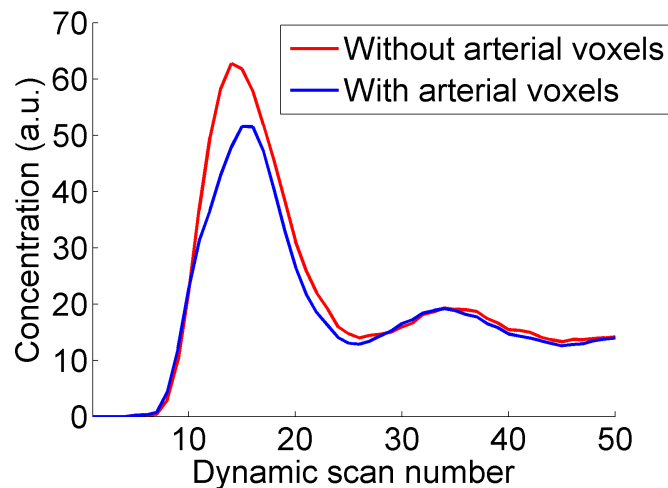
Figure 3.3   The mean CTCs of the clusters before and after modification (i.e. before and after removing the arterial voxels).

The correction factors (AUC_{VOF}/AUC_{CTC}) used for equalizing the time integral of mean CTCs to the venous time integral can be found in Table 3.4.

Table 3.4
The PVE correction factors.

		PAT 1	PAT 2	PAT 3	PAT 4	PAT 5	PAT 6
ROI1	**AIF$_S$**	1.28	1.26	1.17	1.16	1.62	1.57
ROI1	**AIF$_E$**	1.60	1.38	1.71	1.99	1.06	1.04
ROI2	**AIF$_S$**	1.24	1.02	1.00	1.68	1.03	1.87
ROI2	**AIF$_E$**	1.18	1.71	1.18	1.21	1.36	1.15

PAT: Patient, ROI: Region of interest

This study has also shown that the CTCs belonging to voxels mostly located on or anterior to the MCA fail to be AIF. Table 3.5 presents the typical clusters that were rejected to be AIF, their locations with respect to the artery, and SS:AUC values for all patients.

Table 3.5
Rejected clusters (AIF$_E$), their locations, and SS:AUC.

PAT	ROI	SL	CL	CL Region	SS:AUC
1	1	MCA	10	On & anterior	0.0109
1	2	MCA	11	On & anterior & posterior	0.0355
2	1	MCA	9	On & anterior & posterior	0.0149
2	2	MCA	9	Mostly on & posterior	0.0270
3	1	MCA	8	On & distal	0.0146
3	2	MCA	9	On	0.0264
4	1	MCA	9	Mostly on	0.0151
4	2	MCA	9	On & anterior	0.0131
5	1	MCA	8	On	0.0136
5	2	MCA	8	On & anterior	0.0138
6	1	MCA	10	On & anterior	0.0174
6	2	MCA	10	On	0.0094

PAT: Patient, ROI: Region of interest, SL: Slice, CL: Cluster

As we investigated the CTC shape distortions, we came across the typology suggested by Bleeker et al. [16] in unsafe regions of the MCA territory for AIF selection (Figure 3.4).
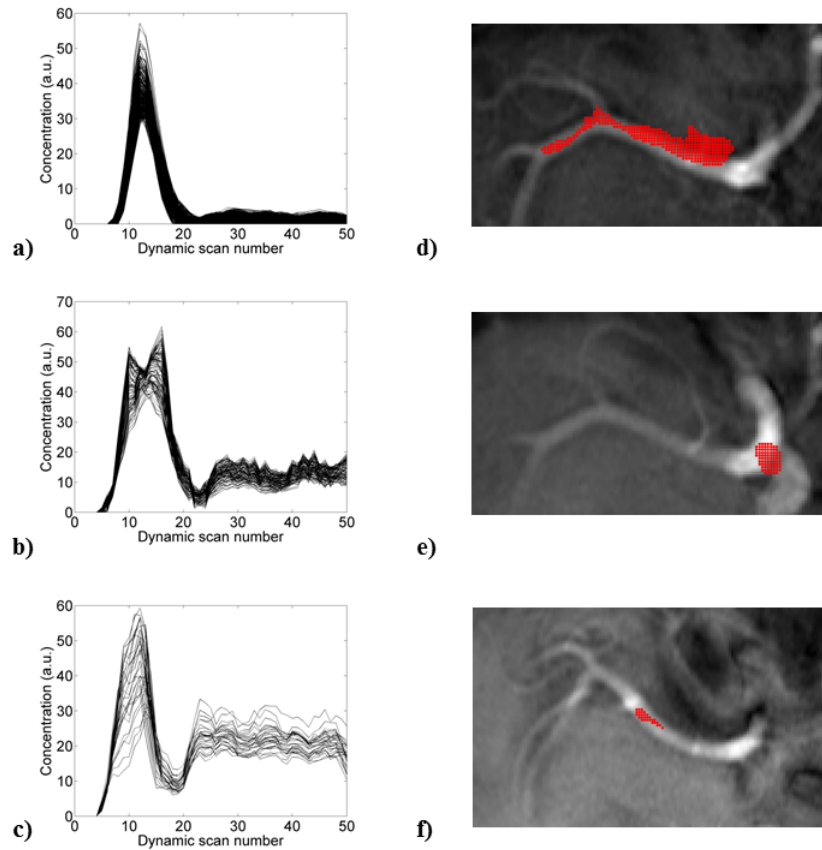
Figure 3.4 CTC shape distortions demonstrated in **a)**, **b)**, and **c)** are derived from voxels shown in **d)**, **e)**, and **f)**. **a)** The higher peaks and smaller FWHMs than the true reference, **b)** two peaks in the first passage of the contrast agent, **c)** no peak in the first passage and a high post-bolus equilibrium, **d)** voxels on and anterior to the MCA, **e)** voxels on the MCA, **f)** voxels on the MCA .

Figure 3.4a exemplifies the first type of shape distortion, where CTCs have high peaks and small FWHMs. Figure 3.4b demonstrates the second type, where the concentration curve is characterized by two peaks in the first passage of the contrast agent. Figure 3.4c shows the third type, which is characterized by an almost undetectable peak in the first passage and a high post-bolus equilibrium.

3.2.2   AIF Clusters

Fuzzy clustering employed for each patient resulted in a different number of clusters (from 9 to 12 across 6 patients), among which we were able to find at least one cluster (AIF cluster) that is close to the reference SS:AUC. Table 3.6 presents the reference SS:AUC values for all patients.

Table 3.6
Reference SS:AUC values for all patients.

	PAT 1	PAT 2	PAT 3	PAT 4	PAT 5	PAT 6
Reference SS:AUC	0.0220	0.0200	0.0211	0.0208	0.0199	0.0192

PAT: Patient

The AIF clusters were examined in terms of their locations with respect to the MCA. AIF clusters' locations ("cluster region") and SS:AUC values are provided in Table 3.7.

Table 3.7
Selected clusters (AIF$_S$), their locations, and SS:AUC.

PAT	ROI	SL	CL	CL Region	SS:AUC
1	1	Superior	11	Superior & posterior	0.0220
1	2	Inferior	12	Inferior	0.0192
2	1	MCA	10	Anterior	0.0208
2	2	Inferior	11	Inferior & posterior	0.0199
3	1	Inferior	10	Inferior & posterior	0.0219
3	2	MCA	9	Mostly posterior & anterior	0.0235*
4	1	Inferior	11	Inferior	0.0200
4	2	Inferior	7	Inferior	0.0200
5	1	Superior	7	Superior & posterior	0.0213
5	2	Inferior	10	Inferior & posterior & anterior	0.0184
6	1	Superior	9	Superior & posterior	0.0206
6	2	MCA	8	Posterior & anterior	0.0191

PAT: Patient, ROI: Region of interest, SL: Slice, CL: Cluster

*SS:AUC is 0.0264 with arterial voxels

The evaluation of cluster regions revealed that the AIF can be found outside the MCA (Figure 3.5).
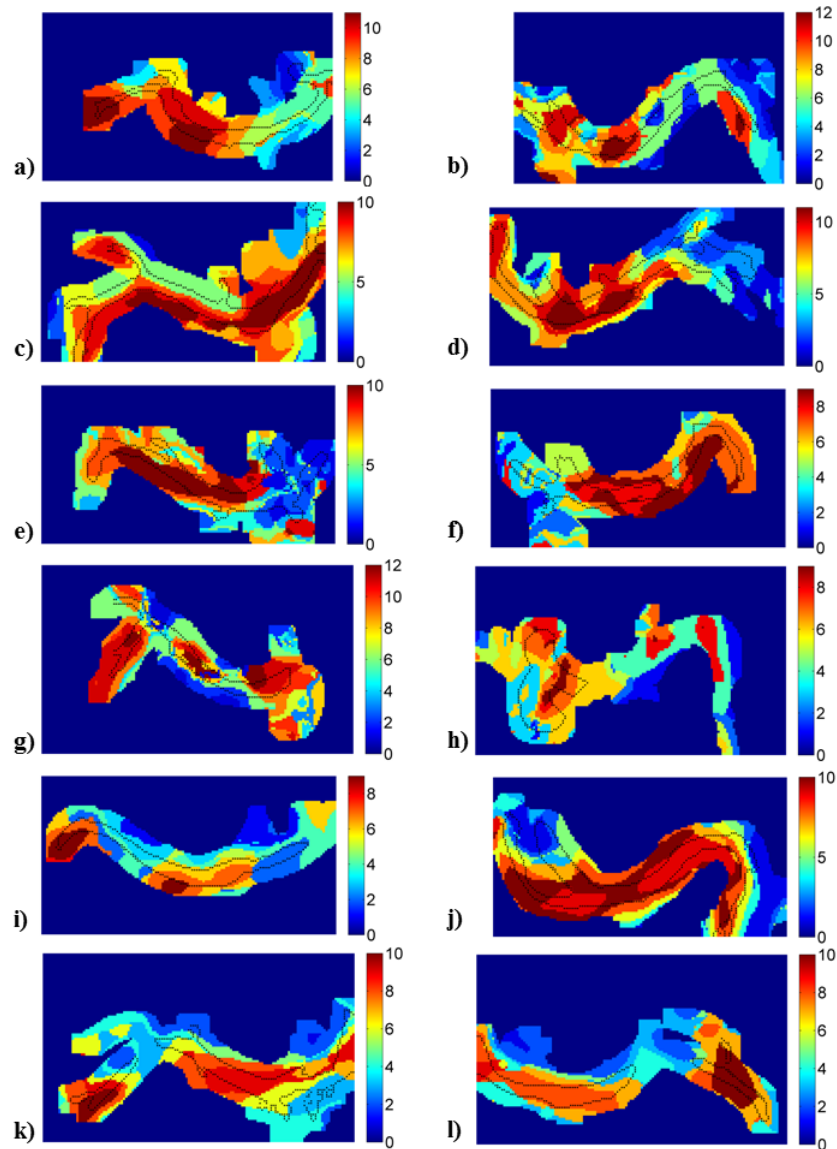
Figure 3.5 Cluster locations of AIF$_S$.
PAT1: **a)** ROI1: CL 11 at superior slice, superior and posterior region of MCA; **b)** ROI2: CL 12 at inferior slice, inferior region of MCA;
PAT2: **c)** ROI1: CL 10 at MCA slice, anterior region of MCA; **d)** ROI2: CL 11 at inferior slice, inferior and posterior region of MCA;
PAT3: **e)** ROI1: CL 10 at inferior slice, inferior and posterior region of MCA; **f)** ROI2: CL 9 at MCA slice, mostly posterior and anterior region of MCA;
PAT4: **g)** ROI1: CL11 at inferior slice, inferior region of MCA; **h)** ROI2: CL 7 at inferior slice, inferior region of MCA;
PAT5: **i)** ROI1: CL7 at superior slice, superior and posterior region of MCA; **j)** ROI2: CL 10 at inferior slice, inferior, posterior and anterior region of MCA;
PAT6: **k)** ROI1: CL 9 at superior slice, superior and posterior region of MCA; **l)** ROI2: CL 8 at MCA slice, posterior and anterior region of MCA.
Color bar indicates the background (dark blue) and cluster numbers .

It was also observed that AIF$_S$s calculated through clustering from ROI1 and ROI2 reveal close similarities in terms of CTC parameters for the patients 2, 4, 5, and

6, whereas they differed significantly for patients 1 and 3.

3.3   CBF Estimation

Figure 3.6 shows AIF_S and AIF_E estimated from ROI1 and ROI2 for all patients, whereas Figure 3.7 presents the CBF maps of a sample brain slice for each case.
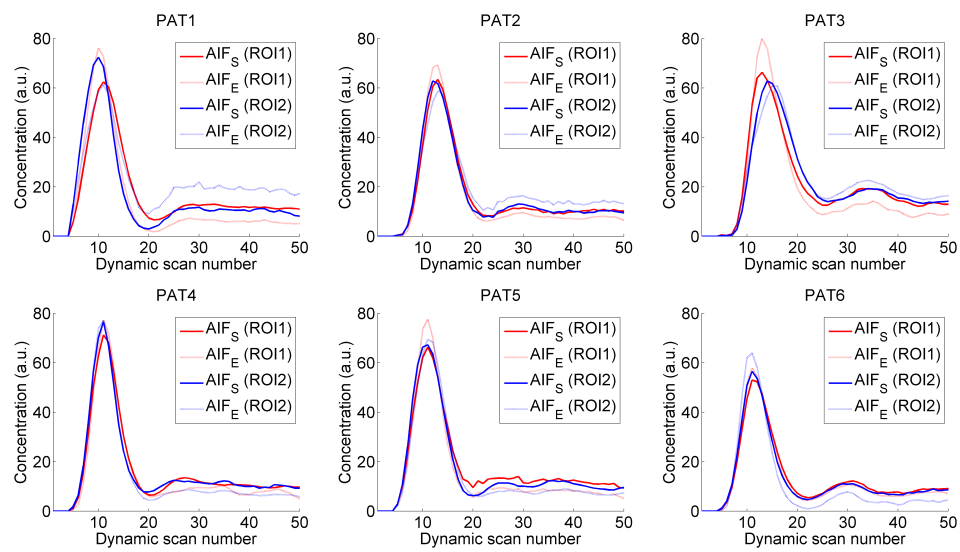
Figure 3.6 AIF_S and AIF_E (from ROI1 and ROI2) of each patient.

.
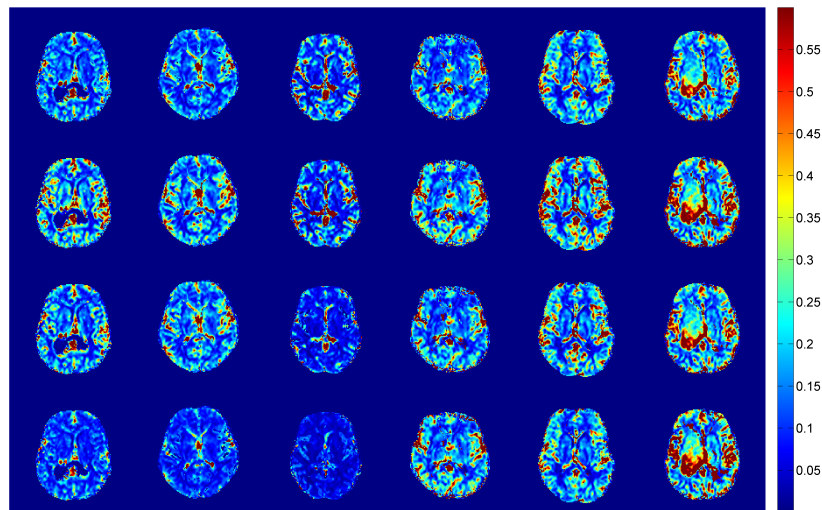
Figure 3.7 CBF maps of a sample brain slice computed using AIF_S from ROI1 (first row), AIF_E from ROI1 (second row), AIF_S from ROI2 (third row), and AIF_E from ROI2 (fourth row).

.

It was found that CBF would be either under- or over-estimated if AIF is far from the reference SS:AUC (see Table 3.8 for CBF percentage differences).

CBF maps calculated using AIF_Ss from ipsilateral and contralateral sides do not have significant differences for patients 2, 4, 5, and 6, whereas they differed significantly for patients 1 and 3.

Table 3.8
CBF percentage differences between using AIF_E and AIF_S.

PAT	ROI	CBF by AIF_E	Mean $\pm$ SD (%)
1	1	Overestimated by	36.6 ± 19.2
1	2	Underestimated by	29.2 ± 16.2
2	1	Overestimated by	25.7 ± 15.2
2	2	Underestimated by	35.2 ± 13.4
3	1	Underestimated by	12.9 ± 11.6
3	2	Underestimated by	41.1 ± 14.3
4	1	Overestimated by	33.1 ± 16.8
4	2	Overestimated by	17.3 ± 11.9
5	1	Overestimated by	31.0 ± 17.8
5	2	Underestimated by	14.1 ± 11.6
6	1	Overestimated by	26.8 ± 15.6
6	2	Overestimated by	23.8 ± 16.4

PAT: Patient, ROI: Region of interest

4. DISCUSSION

The selection of the AIF voxel is an extremely complicated task that requires case-based reasoning [24]. In pathologies such as arterial stenosis or occlusion, where the AIF shape might be distorted due to the delay and dispersion of the contrast agent [34], it is wiser to measure the AIF from a small proximal artery, despite the risk of PVE at some level [18]. In cases with no major arterial abnormalities, where delay and dispersion effects are unlikely or negligible, AIF can be obtained from a large artery, preferably the M1 segment of the middle cerebral artery (MCA), which is advantageous in terms of compromising between PVE and proximity to the tissue [6]. In this study, we similarly focused on this segment of the MCA.

Earlier studies, using manual or automatic AIF selection methods, have referred to certain common CTC criteria. In cases where manual technique is implemented, researchers search for the CTCs that have early, high and narrow peaks in the ROI, where they will determine the mean curve of the voxels as the AIF [51–55]. The manual method is usually criticized for being highly subjective, time consuming and prone to inconsistencies in determining AIF voxels [51–54]. In automatic methods, on the other hand, a search-algorithm is employed to identify the CTCs with high PH, small FWHM, early TTP, and early AT [51–55]. This latter technique might also be misleading since there is always the risk of shape distortions in AIF [59].

The study by Bleeker et al. [16], offering to use the SS:AUC ratio as an additional CTC criterion in order to circumvent PVE, marks a significant progress in the field, however the knowledge of the spatial location of the AIF voxel remains a challenging task for avoiding all other possible causes of shape distortion. The ultimate purpose of this study is to improve AIF selection by utilizing MRA for detecting the arterial locations and dealing with shape distortions. Using MRA images is suggested as a complementary procedure alongside the recognized approaches based on the parametric evaluation of CTCs. This is a promising technique in AIF selection that will enable

radiologists to distinguish the arteries from the surrounding tissue and to specify the arterial location of AIF voxels in a ROI, a task that cannot be accomplished exclusively based on perfusion imaging.

Our AIF selection procedure based on cluster analysis entails both the prevention and correction of shape distortions in the mean CTCs. We eliminated the arterial voxels from clusters to avoid the distortion risk that is associated with problems such as arterial signal saturation at peak concentration, signal relocation during the passage of the contrast agent, and the non-linearity in ΔR2* vs contrast in whole blood. We have found this method more convenient than time consuming manual techniques used for AIF correction. The benefit of removing the arterial voxels became evident when we compared the mean CTCs of the clusters before and after modification (i.e. before and after removing the arterial voxels). It was observed that the SS:AUC ratio of the mean CTC gets closer to the reference value when the arterial voxels are excluded from the cluster.

To correct PVE, we resorted to a common method that normalizes the AIF with respect to the VOF [61]. Thereby, the AUC of the AIF has been increased to prevent overestimation of CBF. Another advantage about the VOF is obtaining a reference value for SS:AUC to be used in AIF decision. The study revealed that significant CBF differences occur between AIFs that are close to and far from the reference SS:AUC, namely AIF_S and AIF_E. The CBF would be under- or overestimated if AIF_E is mistakenly used, which is highly probable when employing manual or automatic AIF selection methods based on conventional CTC parameters regardless of the SS:AUC ratio.

With fuzzy clustering, the study systematically compared the selected and eliminated CTCs based on established parameters with a particular focus on the SS:AUC ratio that has been found critical in eliminating PVE [16]. The parametric evaluations of the CTCs and the angiographic investigation of the related voxels yielded consistent results. Specifically, through MRA we have verified that it is highly crucial to determine the reference SS:AUC value in AIF selection.

Overall, the MRA assessment enabled us to locate the voxels that meet the AIF criteria as well as those with shape distortions. We were able to evaluate both sets of voxels in terms of their positions with regard to the MCA. Our study demonstrated that the voxels of the cluster chosen as AIF are located superior, inferior, posterior or anterior to the MCA, whereas CTC distortions are mostly observed either on or anterior to the MCA. Our findings related to PVE are compatible with the CTC shape distortion typology suggested by Bleeker et al. [16]. In the first type, the CTCs have higher peaks and smaller FWHMs than the true reference. In the second type, two peaks are observed in the first passage of the contrast agent. In the third type, no first pass peak is detected while high SS amplitude is observed.

Angiographic investigation fosters a productive doubt about AIF selection methods that are exclusively based on the CTC parameter analysis. With MRA images at hand, the proposed technique will enable the researchers to exclude the voxels on the MCA during cluster analysis, and to avoid the risk of shape distortions.

5. CONCLUSION

MRA is recommended as a supplementary technique in perfusion imaging to identify the spatial location of an AIF. This imaging technique contributes to quantitative assessment of brain perfusion through improved AIF selection. Accurate CBF quantification is crucial for understanding the extent of brain damages caused by pathologies, including tumors and ischemia. This study ultimately seeks to provide guidance to clinical MR imaging practitioners and healthcare providers who particularly work on the diagnosis and treatment of such cerebral pathologies.

REFERENCES

1. Rosen, B. R., J. W. Belliveau, J. M. Vevea, and T. J. Brady, "Perfusion imaging with NMR contrast agents," *Magnetic Resonance in Medicine*, Vol. 14, no. 2, pp. 249–265, 1990.

2. Donnan, G. A., J. Baron, S. M. Davis, and F. R. Sharp, "The ischemic penumbra: overview, definition, and criteria," *Neurological Disease and Therapy*, Vol. 93, p. 7, 2007.

3. Logothetis, N. K., "What we can do and what we cannot do with fMRI," *Nature*, Vol. 453, no. 7197, pp. 869–878, 2008.

4. Calamante, F., D. L. Thomas, G. S. Pell, J. Wiersma, and R. Turner, "Measuring Cerebral Blood Flow Using Magnetic Resonance Imaging Techniques," *Journal of Cerebral Blood Flow & Metabolism*, Vol. 19, pp. 701–735, jul 1999.

5. Giesel, F. L., A. Mehndiratta, and M. Essig, "High-relaxivity contrast-enhanced magnetic resonance neuroimaging: a review," *European Radiology*, Vol. 20, pp. 2461–2474, oct 2010.

6. Østergaard, L., R. M. Weisskoff, D. A. Chesler, C. Gyldensted, and B. R. Rosen, "High resolution measurement of cerebral blood flow using intravascular tracer bolus passages. Part I: Mathematical approach and statistical analysis," *Magnetic Resonance in Medicine*, Vol. 36, pp. 715–725, nov 1996.

7. Lassen, N., and W. Perl, "Tracer kinetic methods in medical physiology," 1979.

8. Meier, P., K. Z. J. of applied Physiology, and U. 1954, "On the theory of the indicator-dilution method for measurement of blood flow and volume," *American Physiological Society*.

9. Thomas, D., M. Lythgoe, G. Pell, and F. Calamante, "The measurement of diffusion and perfusion in biological systems using magnetic resonance imaging," *Physics in Medicine & Biology*, 2000.

10. Barbier, E. L., L. Lamalle, and M. Décorps, "Methodology of brain perfusion imaging," *Journal of Magnetic Resonance Imaging*, Vol. 13, no. 4, pp. 496–520, 2001.

11. ØStergaard, L., "Cerebral perfusion imaging by bolus tracking," *Topics in Magnetic Resonance Imaging*, Vol. 15, no. 1, pp. 3–9, 2004.

12. Wu, O., L. Østergaard, and A. G. Sorensen, "Technical aspects of perfusion-weighted imaging," *Neuroimaging Clinics of North America*, Vol. 15, no. 3, pp. 623–637, 2005.

13. Calamante, F., S. Christensen, P. M. Desmond, L. Østergaard, S. M. Davis, and A. Connelly, "The physiological significance of the time-to-maximum (Tmax) parameter in perfusion MRI," *Stroke*, Vol. 41, no. 6, pp. 1169–1174, 2010.

14. Knutsson, L., F. Ståhlberg, and R. Wirestam, "Absolute quantification of perfusion using dynamic susceptibility contrast MRI: Pitfalls and possibilities," 2010.

15. Willats, L., and F. Calamante, "The 39 steps: Evading error and deciphering the secrets for accurate dynamic susceptibility contrast MRI," *NMR in Biomedicine*, Vol. 26, no. 8, pp. 913–931, 2013.

16. Bleeker, E. J. W., M. J. P. Van Osch, A. Connelly, M. A. Van Buchem, A. G. Webb, and F. Calamante, "New criterion to aid manual and automatic selection of the arterial input function in dynamic susceptibility contrast MRI," *Magnetic Resonance in Medicine*, Vol. 65, no. 2, pp. 448–456, 2011.

17. Bleeker, E. J., M. A. Van Buchem, and M. Jp Van Osch, "Optimal location for arterial input function measurements near the middle cerebral artery in first-pass perfusion MRI," *Journal of Cerebral Blood Flow & Metabolism*, Vol. 29155, no. 10, pp. 840–852, 2009.

18. Calamante, F., "Arterial input function in perfusion MRI: a comprehensive review," *Progress in Nuclear Magnetic Resonance Spectroscopy*, Vol. 74, pp. 1–32, 2013.

19. Weisskoff, R. M., D. Chesler, J. L. Boxerman, and B. R. Rosen, "Pitfalls in MR measurement of tissue blood flow with intravascular tracers: Which mean transit time?," *Magnetic Resonance in Medicine*, Vol. 29, no. 4, pp. 553–558, 1993.

20. Perthen, J. E., F. Calamante, D. G. Gadian, and A. Connelly, "Is quantification of bolus tracking MRI reliable without deconvolution?," *Magnetic Resonance in Medicine*, Vol. 47, no. 1, pp. 61–67, 2002.

21. Calamante, F., D. G. Gadian, and A. Connelly, "Quantification of Bolus-Tracking MRI: Improved Characterization of the Tissue Residue Function Using Tikhonov Regularization," *Magnetic Resonance in Medicine*, Vol. 50, no. 6, pp. 1237–1247, 2003.

22. Van Osch, M. J. P., E. J. P. A. Vonken, O. Wu, M. A. Viergever, J. Van der Grond, and C. J. G. Bakker, "Model of the human vasculature for studying the influence of contrast injection speed on cerebral perfusion MRI," *Magnetic Resonance in Medicine*, Vol. 50, no. 3, pp. 614–622, 2003.

23. Grüner, R., and T. Taxt, "Iterative blind deconvolution in magnetic resonance brain perfusion imaging," *Magnetic Resonance in Medicine*, Vol. 55, no. 4, pp. 805–815, 2006.

24. Calamante, F., D. G. Gadian, and A. Connelly, "Delay and dispersion effects in dynamic susceptibility contrast MRI: simulations using singular value decomposition.," *Magnetic Resonance in Medicine*, Vol. 44, no. 3, pp. 466–73, 2000.

25. Wu, O., L. Østergaard, R. M. Weisskoff, T. Benner, B. R. Rosen, and A. G. Sorensen, "Tracer arrival timing-insensitive technique for estimating flow in MR perfusion-weighted imaging using singular value decomposition with a block-circulant deconvolution matrix," *Magnetic Resonance in Medicine*, Vol. 50, no. 1, pp. 164–174, 2003.

26. Andersen, I. K., A. Szymkowiak, C. E. Rasmussen, L. G. Hanson, J. R. Marstrand, H. B. W. Larsson, and L. K. Hansen, "Perfusion quantification using Gaussian process deconvolution," *Magnetic Resonance in Medicine*, Vol. 48, no. 2, pp. 351–361, 2002.

27. Liu, H. L., Y. Pu, Y. Liu, L. Nickerson, T. Andrews, P. T. Fox, and J. H. Gao, "Cerebral blood flow measurement by dynamic contrast MRI using singular value decomposition with an adaptive threshold.," *Magnetic Resonance in Medicine*, Vol. 42, no. 1, pp. 167–172, 1999.

28. Christensen, S., F. Calamante, N. Hjort, O. Wu, A. D. Blankholm, P. Desmond, S. Davis, and L. Østergaard, "Inferring origin of vascular supply from tracer arrival timing patterns using bolus tracking MRI," *Journal of Magnetic Resonance Imaging*, Vol. 27, no. 6, pp. 1371–1381, 2008.

29. Knutsson, L., F. Ståhlberg, and R. Wirestam, "Aspects on the accuracy of cerebral perfusion parameters obtained by dynamic susceptibility contrast MRI: A simulation study," *Magnetic Resonance Imaging*, Vol. 22, no. 6, pp. 789–798, 2004.

30. Calamante, F., and A. Connelly, "Perfusion precision in bolus-tracking MRI: Estimation using the wild-bootstrap method," *Magnetic Resonance in Medicine*, Vol. 61, no. 3, pp. 696–704, 2009.

31. Thompson, H. K., C. F. Starmer, R. E. Whalen, and H. D. Mcintosh, "Indicator Transit Time Considered as a Gamma Variate," *Circulation Research*, Vol. 14, no. 6, pp. 502–515, 1964.

32. Davenport, R., "The derivation of the gamma-variate relationship for tracer dilution curves.," *Journal of Nuclear Medicine*, Vol. 24, no. 10, pp. 945–8, 1983.

33. Calamante, F., V. Ganesan, F. J. Kirkham, W. Jan, W. K. Chong, D. G. Gadian, and A. Connelly, "MR perfusion imaging in moyamoya syndrome," *Stroke*, Vol. 32, no. 12, pp. 2810–2816, 2001.

34. Calamante, F., D. G. Gadian, and A. Connelly, "Quantification of perfusion using bolus tracking magnetic resonance imaging in stroke," *Stroke*, Vol. 33, no. 4, pp. 1146–1151, 2002.

35. Lorenz, C., T. Benner, C. J. Lopez, H. Ay, M. W. Zhu, H. Aronen, J. Karonen, Y. Liu, J. Nuutinen, and A. Gregory Sorensen, "Effect of using local arterial input functions on cerebral blood flow estimation," *Journal of Magnetic Resonance Imaging*, Vol. 24, no. 1, pp. 57–65, 2006.

36. Lorenz, C., T. Benner, P. J. Chen, C. J. Lopez, H. Ay, M. W. Zhu, N. M. Menezes, H. Aronen, J. Karonen, and Y. Liu, "Automated perfusion-weighted MRI using localized arterial input functions," *Journal of Magnetic Resonance Imaging*, Vol. 24, no. 5, pp. 1133–1139, 2006.

37. Knutsson, L., E. M. Larsson, O. Thilmann, F. Ståhlberg, and R. Wirestam, "Calculation of cerebral perfusion parameters using regional arterial input functions identified by factor analysis," *Journal of Magnetic Resonance Imaging*, Vol. 23, no. 4, pp. 444–453, 2006.

38. Willats, L., A. Connelly, and F. Calamante, "Minimising the effects of bolus dispersion in bolus-tracking MRI," *NMR in Biomedicine*, Vol. 21, no. 10, pp. 1126–1137, 2008.

39. Willats, L., S. Christensen, H. K Ma, G. A Donnan, A. Connelly, and F. Calamante, "Validating a local Arterial Input Function method for improved perfusion quantification in stroke," *Journal of Cerebral Blood Flow and Metabolism*, Vol. 31, no. 11, pp. 2189–2198, 2011.

40. Grüner, R., and T. Taxt, "Cepstral estimation of arterial input functions in brain perfusion imaging," *Journal of Magnetic Resonance Imaging*, Vol. 26, no. 3, pp. 773–779, 2007.

41. Lee, J. J., G. L. Bretthorst, C. P. Derdeyn, W. J. Powers, T. O. Videen, A. Z. Snyder, J. Markham, and J. S. Shimony, "Dynamic susceptibility contrast MRI with localized arterial input functions," *Magnetic Resonance in Medicine*, Vol. 63, no. 5, pp. 1305–1314, 2010.

42. Calamante, F., M. Mørup, and L. K. Hansen, "Defining a local arterial input function for perfusion MRI using independent component analysis," *Magnetic Resonance in Medicine*, Vol. 52, no. 4, pp. 789–797, 2004.

43. Bleeker, E. J. W., A. G. Webb, M. A. A. Van Walderveen, M. A. Van Buchem, and M. J. P. Van Osch, "Evaluation of signal formation in local arterial input function measurements of dynamic susceptibility contrast MRI," *Magnetic Resonance in Medicine*, Vol. 67, no. 5, pp. 1324–1331, 2012.

44. Ebinger, M., P. Brunecker, G. J. Jungehülsing, U. Malzahn, C. Kunze, M. Endres, and J. B. Fiebach, "Reliable perfusion maps in stroke MRI using arterial input functions derived from distal middle cerebral artery branches," *Stroke*, Vol. 41, no. 1, pp. 95–101, 2010.

45. Sorensen, A., and P. Reimer, "Cerebral MR perfusion imaging: principles and current applications," 2000.

46. Weisskoff, R., S. Chun, J. Boxerman, and B. Rosen, "Microsocopic susceptiblity variation and transverse relaxation: Theory and experiment," *Magnetic Resonance in Medicine*, Vol. 31, no. 29, pp. 601–610, 1994.

47. Boxerman, J. L., L. M. Hamberg, B. R. Rosen, and R. M. Weisskoff, "MR contrast due to intravascular magnetic susceptibility perturbations," *Magnetic Resonance in Medicine*, Vol. 34, no. 4, pp. 555–566, 1995.

48. Thulborn, K. R., S. Y. Chang, G. X. Shen, and J. T. Voyvodic, "High-resolution echo-planar fMRI of human visual cortex at 3.0 tesla.," *NMR in Biomedicine*, Vol. 10, pp. 183–190, 1997.

49. Wintermark, M., G. Albers, A. Alexandrov, J. Alger, R. Bammer, J.-C. Baron, S. Davis, B. Demaerschalk, C. Derdeyn, G. Donnan, J. Eastwood, J. Fiebach, M. Fisher, K. Furie, G. Goldmakher, W. Hacke, C. Kidwell, S. Kloska, M. Köhrmann, W. Koroshetz, T.-Y. Lee, K. Lees, M. Lev, D. Liebeskind, L. Ostergaard, W. Powers, J. Provenzale, P. Schellinger, R. Silbergleit, A. Sorensen, J. Wardlaw, O. Wu, and S. Warach, "Acute stroke imaging research roadmap," *Stroke*, Vol. 39, no. 5, 2008.

50. Vonken, E. J., M. J. van Osch, C. J. Bakker, and M. A. Viergever, "Measurement of cerebral perfusion with dual-echo multi-slice quantitative dynamic susceptibility contrast MRI," *Journal of Magnetic Resonance Imaging*, Vol. 10, no. 2, pp. 109–117, 1999.

51. Mlynash, M., I. Eyngorn, R. Bammer, M. Moseley, and D. C. Tong, "Automated method for generating the arterial input function on perfusion-weighted MR imaging: validation in patients with stroke," *American Journal of Neuroradiology*, Vol. 26, no. 6, pp. 1479–1486, 2005.

52. Mouridsen, K., S. Christensen, L. Gyldensted, and L. Ostergaard, "Automatic selection of arterial input function using cluster analysis," *Magnetic Resonance in Medicine*, Vol. 55, no. 3, pp. 524–531, 2006.

53. Carroll, T. J., H. A. Rowley, and V. M. Haughton, "Automatic Calculation of the Arterial Input Function for Cerebral Perfusion Imaging with MR Imaging," *Radiology*, Vol. 227, no. 2, pp. 593–600, 2003.

54. Murase, K., K. Kikuchi, H. Miki, T. Shimizu, and J. Ikezoe, "Determination of arterial input function using fuzzy clustering for quantification of cerebral blood flow with dynamic susceptibility contrast-enhanced MR imaging," *Journal of Magnetic Resonance Imaging*, Vol. 13, no. 5, pp. 797–806, 2001.

55. Bjørnerud, A., and K. E. Emblem, "A fully automated method for quantitative cerebral hemodynamic analysis using DSC-MRI," *Journal of Cerebral Blood Flow & Metabolism*, Vol. 30, no. 5, pp. 1066–1078, 2010.

56. Kim, J., E. C. Leira, R. C. Callison, B. Ludwig, T. Moritani, V. A. Magnotta, and M. T. Madsen, "Toward fully automated processing of dynamic susceptibility contrast perfusion MRI for acute ischemic cerebral stroke," *Computer Methods and Programs in Biomedicine*, Vol. 98, no. 2, pp. 204–213, 2010.

57. Straka, M., G. W. Albers, and R. Bammer, "Real-time diffusion-perfusion mismatch analysis in acute stroke," 2010.

58. Galinovic, I., P. Brunecker, A. C. Ostwaldt, C. Soemmer, B. Hotter, and J. B. Fiebach, "Fully automated postprocessing carries a risk of substantial overestimation of perfusion deficits in acute stroke magnetic resonance imaging," *Cerebrovascular Diseases*, Vol. 31, no. 4, pp. 408–413, 2011.

59. Van Osch, M. J. P., J. Van Der Grond, and C. J. G. Bakker, "Partial volume effects on aterial input functions: Shape and amplitude distortions and their correction," *Journal of Magnetic Resonance Imaging*, Vol. 22, no. 6, pp. 704–709, 2005.

60. Pedersen, M., M. Klarhöfer, S. Christensen, J. C. Ouallet, L. Østergaard, V. Dousset, and C. Moonen, "Quantitative cerebral perfusion using the PRESTO acquisition scheme," *Journal of Magnetic Resonance Imaging*, Vol. 20, no. 6, pp. 930–940, 2004.

61. Foottit, C., G. O. Cron, M. J. Hogan, T. B. Nguyen, and I. Cameron, "Determination of the venous output function from MR signal phase: Feasibility for quantitative DCE-MRI in human brain," *Magnetic Resonance in Medicine*, Vol. 63, no. 3, pp. 772–781, 2010.

62. Sourbron, S., R. Luypaert, P. Van Schuerbeek, M. Dujardin, and T. Stadnik, "Choice of the regularization parameter for perfusion quantification with MRI," *Physics in Medicine and Biology*, Vol. 49, no. 14, pp. 3307–3324, 2004.

63. Hansen, P. C., "Analysis of Discrete Ill-Posed Problems by Means of the L-Curve," *SIAM Review*, Vol. 34, no. 4, pp. 561–580, 1992.